Asymptotic expansion and Padé approximants for gravity-driven flow of a heated granular gas: Competition between inelasticity and forcing, up to Burnett order

Ramakrishna Rongali and Meheboob Alam*

Engineering Mechanics Unit, Jawaharlal Nehru Centre for Advanced Scientific Research, Jakkur P.O., Bangalore 560064, India

(Received 13 August 2018; published 29 November 2018)

The gravity-driven planar channel flow of a heated granular gas is analyzed using a kinetic model with stochastic forcing to understand the roles of inelasticity and forcing on its hydrodynamics and rheology. The closed-form analytical solutions up to the fourth order in gravitational acceleration have been determined to analyze the hydrodynamic and rheological fields as functions of the restitution coefficient (e_n) and the Froude number Fr_0. It is found that the excess temperature [$\Delta T = T_{\max}/T(0) - 1$, i.e., the deviation of the maximum temperature $T_{\max}$ of the gas from its centerline value $T(0)$] increases monotonically with decreasing e_n above a critical value of the Froude number ($\mathrm{Fr}_0 > \mathrm{Fr}_0^c$), but has a "nonmonotonic" dependence with e_n [i.e., ΔT decreases with decreasing e_n for $e_n \in (1, 0.5)$, but increases for $e_n < 0.5$] at $\mathrm{Fr}_0 < \mathrm{Fr}_0^c$. This changeover from nonmonotonic to monotonic dependence of ΔT with e_n at $\mathrm{Fr}_0 = \mathrm{Fr}_0^c$ also holds for both first ($\mathcal{N}_1$) and second ($\mathcal{N}_2$) normal-stress differences as well as for tangential heat flux (q_x). Phase diagrams are constructed in the (Fr_0, $1 - e_n$) plane, demarcating two regions in which the dependencies of rarefaction effects (ΔT, $\mathcal{N}_1$, $\mathcal{N}_2$, and q_x) on e_n are monotonic and nonmonotonic. The inelasticity plays a "dual" role of decreasing (at $\mathrm{Fr}_0 < \mathrm{Fr}_0^c$) and increasing (at $\mathrm{Fr}_0 > \mathrm{Fr}_0^c$) the rarefaction effects with decreasing restitution coefficient e_n from the elastic limit. This finding, based on the fourth-order solution, is in variance with the leading-order solution that predicts only a nonmonotonic dependence of the above quantities on e_n for all Fr_0 [Tij and Santos, J. Stat. Phys. **117**, 901 (2004)]. The role of inelasticity on the region of convergence of the asymptotic series solutions are subsequently analyzed by determining the Padé approximants for rheological fields [Rongali and Alam, Phys. Rev. E **98**, 012115 (2018)]; the present solution is shown to have a larger range of validity in terms of both inelasticity and Froude number than its leading-order counterpart. Lastly, it is shown that the fourth-order solutions contain all Burnett-order terms (i.e., second order in the gradients of hydrodynamic fields) that can be obtained from the standard Chapman-Enskog expansion.

DOI: 10.1103/PhysRevE.98.052144

I. INTRODUCTION

Kinetic theory ideas and the Boltzmann equation are commonly used to analyze various properties of dilute gases [1–8]; the latter is a nonlinear integrodifferential equation for the spatiotemporal evolution of the single-particle distribution function, which admits an exact solution for the "rest" state of a gas in the form of the Maxwell-Boltzmann distribution function which serves to derive the equation of state of a gas. For gaseous flows, satisfying the molecular chaos assumption (Boltzmann's stosszahlansatz [2]), the range of validity of the Boltzmann equation spans all values of Knudsen numbers ($\mathrm{Kn} = \lambda/L$, the ratio between the mean-free path of gas molecules to macroscopic length scale [9]), ranging from the continuum regime ($\mathrm{Kn} \sim 0$) to rarefied regime ($0.01 < \mathrm{Kn} < 10$, which includes both slip-flow and transition-flow regime [6]) to the free molecular limit ($\mathrm{Kn} > 10$). In the continuum regime, various flow phenomena are well described by the Euler and Navier-Stokes-type continuum equations [3]; the latter hydrodynamic equations are formally derived from the Boltzmann equation via coarse graining over velocity space, with the related flux laws and transport coefficients obtained by employing asymptotic expansion techniques like the Chapman-Enskog expansion [3,4]. In the rarefied regime, however, the higher-order equations in the form of (i) Burnett or super-Burnett [4] equations and/or (ii) the moment equations of Grad [5] are found to be appropriate to tackle various noncontinuum effects [6,7]. For example, the well-known Knudsen paradox [9] (i.e., the nonmonotonic variation of the mass-flow rate of a pressure-driven gas, flowing through a tube, with Knudsen number) has been explained from the Boltzmann equation [10] as well as from "beyond" Navier-Stokes equations [8]. The pressure-driven flow of a gas can also be analyzed by replacing the pressure-gradient by an external force, like gravitational acceleration [7,11–14]. An overview of various noncontinuum or rarefaction effects in the gravity-driven Poiseuille flow of a molecular gas can be found in a recent work [15].

This paper deals with the gravity-driven flow of a granular gas in the dilute regime; see Fig. 1 for typical profiles of hydrodynamic velocity, temperature, and normal heat flux. A picture of granular flows in the rapid flow regime [16], a granular gas, is reminiscent of a molecular gas in many aspects: (i) the collisions are assumed to be binary and instantaneous, but (ii) the crucial difference is that the particles are dissipative; i.e., the particle-particle collisions are

*meheboob@jncasr.ac.in

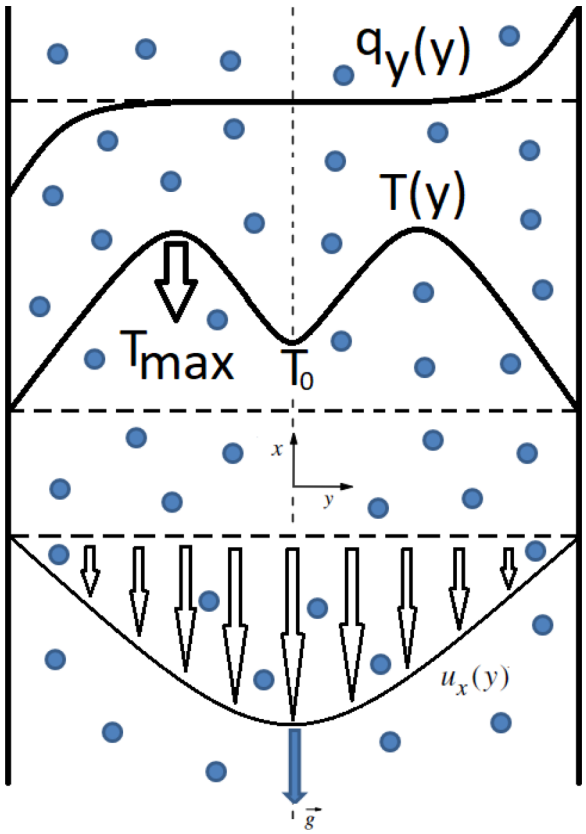

FIG. 1. Schematic of the flow of granular particles, representing a gas, flowing through a plane channel; the flow is driven by gravitational acceleration g acting along the $-x$ direction (streamwise), and y denotes the wall-normal (transverse) direction. Typical transverse profiles of velocity $u_x(y)$, temperature $T(y)$, and normal heat flux $q_y(y)$ are depicted for a rarefied molecular gas. The temperature profile has a "bimodal" shape, with a local minimum at the channel center and two symmetrically located maxima away from the centerline. Interestingly, the heat flows [i.e., $q_y > 0$, or, < 0 for $y > 0$, or, $y < 0$, respectively] from the channel center towards the walls, even though the temperature is minimum at $y = 0$, in contradiction to the Fourier law [i.e., $q_y \propto -(dT/dy)$].

inelastic, characterized by a normal coefficient of restitution, $0 < e_n < 1$, with $e_n = 1$ being identified with the molecular gas. The inelasticity of particle collisions can be incorporated in the Boltzmann equation via its collision integral; however, the time reversibility of the collision integral is lost [16] due to the dissipative nature of collisions and the rest state is no longer an equilibrium state, implying that the Maxwellian is not an equilibrium distribution function for a granular or dissipative gas. Indeed, the ideas of kinetic theory have been extended to dissipative granular particles [17–19] to develop a sound theoretical understanding of the rapid granular flow over the last three decades [19–27]; the readers are referred to a review article [16] and a textbook [28] for various issues on the kinetic theory of granular gases.

The bulk hydrodynamics and rheology for the gravity-driven flow of a granular gas are analyzed in this paper using the tools of kinetic theory and asymptotic expansion. Figure 1 shows the schematic of the planar channel flow in which the granular gas is confined between two infinite parallel plates normal to the y axis; the flow is driven by the gravitational acceleration, i.e., a constant gravitational force per unit mass $\boldsymbol{g} = -g\hat{\boldsymbol{x}}$, along the direction $\hat{\boldsymbol{x}}$ parallel to the plates. One motivation of the present work is to understand certain differences between (i) the theoretical work of Tij and Santos [29,30] and (ii) the molecular dynamics (MD) simulation work of Alam *et al.* [31] and the DSMC (direct simulation Monte Carlo) results of Gupta and Alam [32]; for example, while both MD and DSMC simulations suggest a monotonic increase of the excess temperature (i.e., $\Delta T = T_{\max}/T_0 - 1$; see Fig. 1) with decreasing restitution coefficient, second-order theory [29] predicts its "nonmonotonic" variation in the same limit. Following the work of Tij and Santos [29], the effect of gravity is incorporated perturbatively around a "uniform" state of constant temperature and density which is achieved by a balance between the collisional cooling due to inelastic collisions and a bulk heating mechanism due to white noise. The higher-order solutions are derived which are then used to analyze various rarefaction effects [such as the bimodal shape of the temperature profile (Fig. 1), normal stress differences, and tangential heat flux] in this flow. Three major goals of the present work are to (i) understand how the predictions based on higher-order solutions differ from its leading-order solution, (ii) analyze the convergence properties of the underlying series solutions as done recently by us [15] for a molecular gas, and (iii) verify the connection (if any) between the gravity-based perturbation expansion [12,15,29] with the well-known Kn-based Chapman-Enskog expansion in which the gradients of hydrodynamic fields (proportional to Kn) are treated as small parameters. Unlike in the acceleration-driven Poiseuille flow of a molecular gas for which both the leading- and higher-order solutions give qualitatively similar results [15], the present case of a granular gas yielded surprising results when the higher-order terms are included. In particular we shall show that the macroscopic properties of granular Poiseuille flow are strongly influenced by a competition between inelastic dissipation and external forcing: the inelastic dissipation competes with white-noise forcing if the gravitational acceleration is small enough, but the white-noise forcing plays a passive role beyond a minimum value of the gravitational acceleration.

A brief overview of the kinetic theory of a "heated" granular gas is provided in Sec. II, along with a description of the white-noise heating and a BGK-like kinetic model as well as the reduced kinetic and hydrodynamics equations for the gravity-driven channel flow. In Sec. III the perturbation expansion is outlined, along with explicit solutions at leading and higher orders. Based on present results, the temperature bimodality is discussed in detail in Sec. IV and the rheology in Sec. V. In Sec. VI A the Padé-approximated solution for the rheological quantities are derived and compared with respective leading- and higher-order solutions; the similarities and differences of the present theoretical predictions with respect to existing simulations are discussed in Sec. VI B. The equivalence of the present fourth-order solutions with the well-known Chapman-Enskog solution is discussed in Sec. VII. A brief summary of all results and conclusions is given in Sec. VIII.

II. OVERVIEW ON A HEATED GRANULAR GAS: BOLTZMANN EQUATION, KINETIC MODEL, AND BALANCE LAWS

Referring to Fig. 1, we consider a collection of smooth inelastic hard spheres of mass m and diameter σ that interact via binary collisions, representing a model of a granular gas, flowing down a planar channel under the action of gravity [31–36]. The collisions in a granular gas are inelastic, unlike in a molecular gas, and are characterized by the relation $(\boldsymbol{c}_{01}\cdot\hat{\boldsymbol{\sigma}})=-e_n(\boldsymbol{c}'_{01}\cdot\hat{\boldsymbol{\sigma}})$, where $\boldsymbol{c}_{01}=\boldsymbol{c}-\boldsymbol{c}_1$ and $\boldsymbol{c}'_{01}=\boldsymbol{c}'-\boldsymbol{c}'_1$ denote the relative velocities of a colliding pair of particles before and after a collision, respectively, and $e_n\in[0,1]$ is the coefficient of normal restitution, with $e_n=1$ and 0 representing perfectly elastic and sticky collisions, respectively. The evolution of the single-particle distribution function $f(\boldsymbol{x},\boldsymbol{c};t)$ is governed by the inelastic Boltzmann equation [16,29]

$$\left(\frac{\partial}{\partial t}+\boldsymbol{c}\cdot\nabla+\boldsymbol{g}\cdot\frac{\partial}{\partial\boldsymbol{c}}+\mathscr{F}\right)f=J[f,f], \tag{1}$$

where $\boldsymbol{g}$ is the gravitational acceleration and $J[f,f]$ is the Boltzmann collision integral which depends on the two-body distribution function whose explicit form will be considered in Sec. II B. In Eq. (1), the operator $\mathscr{F}$ is added so that a nonequilibrium uniform or steady state can be achieved for a granular gas by balancing its inherent collisional energy loss with the addition of some heating mechanism; certain properties of $\mathscr{F}$ are described below.

The velocity moments of zeroth, first, and second order, respectively, of Eq. (1) yield

$$\left(\frac{\partial}{\partial t}+\boldsymbol{u}\cdot\nabla\right)\rho+\rho\nabla\cdot\boldsymbol{u}=0, \tag{2a}$$

$$\left(\frac{\partial}{\partial t}+\boldsymbol{u}\cdot\nabla\right)\boldsymbol{u}+\frac{1}{\rho}\nabla\cdot\boldsymbol{P}=\boldsymbol{g}, \tag{2b}$$

$$\left(\frac{\partial}{\partial t}+\boldsymbol{u}\cdot\nabla\right)T+\frac{2}{3n}(\nabla\cdot\boldsymbol{q}+\boldsymbol{P}:\nabla\boldsymbol{u})=-(\zeta-\gamma)T, \tag{2c}$$

which represent the balance equations for mass density (ρ), momentum density, and granular energy, defined via

$$\begin{pmatrix}\rho(\boldsymbol{x},t)=mn(\boldsymbol{x},t)\\ n(\boldsymbol{x},t)\boldsymbol{u}(\boldsymbol{x},t)\\ n(\boldsymbol{x},t)T(\boldsymbol{x},t)\end{pmatrix}=\int d\boldsymbol{c}\begin{pmatrix}m\\ \boldsymbol{c}\\ \frac{m}{3}C^2\end{pmatrix}f(\boldsymbol{x},\boldsymbol{c};t), \tag{3}$$

where $\boldsymbol{C}=\boldsymbol{c}-\boldsymbol{u}$ is the peculiar velocity, $n(\boldsymbol{x},t)$ is the number density, $\boldsymbol{u}(\boldsymbol{x},t)$ is the hydrodynamic velocity, and $T(\boldsymbol{x},t)$ is the granular temperature. In Eq. (2), $\boldsymbol{P}(\boldsymbol{x},t)$ and $\boldsymbol{q}(\boldsymbol{x},t)$ represent the pressure tensor and the heat flux vector, respectively, defined via

$$P_{\alpha\beta}(\boldsymbol{x},t)=m\int d\boldsymbol{c}\,C_\alpha C_\beta f(\boldsymbol{x},\boldsymbol{c};t), \tag{4}$$

$$q_\alpha(\boldsymbol{x},t)=\frac{m}{2}\int d\boldsymbol{c}\,C^2C_\alpha f(\boldsymbol{x},\boldsymbol{c};t). \tag{5}$$

The term $\zeta(\boldsymbol{x},t)$ in the energy equation represents the rate of cooling (per unit volume) due to inelastic collisions and $\gamma(\boldsymbol{x},t)$ represents the heating rate associated with the external driving $\mathscr{F}$; the integral expressions for these two quantities are given by

$$\zeta(\boldsymbol{x},t)=-\frac{m}{3n(\boldsymbol{x},t)T(\boldsymbol{x},t)}\int d\boldsymbol{c}\,C^2J[f,f], \tag{6}$$

$$\gamma(\boldsymbol{x},t)=-\frac{m}{3n(\boldsymbol{x},t)T(\boldsymbol{x},t)}\int d\boldsymbol{c}\,C^2\mathscr{F}f(\boldsymbol{x},\boldsymbol{c};t). \tag{7}$$

The choice of the external heating operator $\mathscr{F}$ is such that it does not alter the mass and momentum balance laws; in other words, the action of $\mathscr{F}$ must preserve the local number density and momentum density, i.e.,

$$\int d\boldsymbol{c}\mathscr{F}f(\boldsymbol{x},\boldsymbol{c};t)=\int d\boldsymbol{c}\,\boldsymbol{c}\mathscr{F}f(\boldsymbol{x},\boldsymbol{c};t)=0. \tag{8}$$

By approximating the actual velocity distribution function by its local Maxwellian

$$f_M(\boldsymbol{x},\boldsymbol{c};t)=n(\boldsymbol{x},t)\left[\frac{m}{2\pi T(\boldsymbol{x},t))}\right]^{3/2}\times\exp\left[-\frac{m[\boldsymbol{c}-\boldsymbol{u}(\boldsymbol{x},t)]^2}{2T(\boldsymbol{x},t)}\right], \tag{9}$$

the leading-order expression for the cooling rate [Eq. (6)] is obtained as

$$\zeta_M(\boldsymbol{x},t)=\tfrac{5}{12}\left(1-e_n^2\right)\nu(\boldsymbol{x},t), \tag{10}$$

with ν being the collision frequency

$$\nu=\frac{16}{5}n\sigma^2\sqrt{\frac{\pi T}{m}}. \tag{11}$$

For perfectly elastic collisions the cooling rate vanishes and no external energy needs to be injected into the system, i.e., $\gamma=0$.

A. Bulk heating mechanism and the gravity-driven Poiseuille flow

Unlike in molecular gases for which the rest state serves as an equilibrium state of constant density and temperature with a Maxwellian distribution function, there is no equilibrium state in a granular gas due to the continual energy loss. However, a steady uniform state can be achieved in a granular gas if it is continually heated via some external energy source such that the energy input balances the collisional loss due to the inelasticity of particles. From a theoretical perspective, the most common type of bulk driving mechanism for inelastic particles contains a stochastic force in the form of Gaussian white noise; for more details on the Gaussian white noise, the reader is referred to Refs. [22,29]. The operator $\mathscr{F}$ associated with the Gaussian white noise appearing in the Boltzmann equation (1) is given by [22,29]

$$\mathscr{F}=-\frac{\xi^2}{2}\left(\frac{\partial}{\partial\boldsymbol{c}}\right)^2, \tag{12}$$

where ξ^2 represents the strength of the white-noise correlation and the term $\xi^2/2$ acts as a diffusion coefficient in the velocity space. The external heating operator (12) satisfies the properties listed in Eq. (8), and inserting Eq. (12) into

Eq. (7) yields an expression for the heating rate $\gamma = m\xi^2/T$. Since the energy loss due to inelastic collisions is assumed to balance the bulk heating due to white-noise forcing, we have $\xi = \sqrt{\zeta T/m}$ at every point.

By considering the above white-noise forcing and in the presence of gravitational acceleration (see Fig. 1), a steady state can be expected in which the physical quantities depend on the transverse coordinate y only and the flow velocity is parallel to the x axis, i.e., $\boldsymbol{u} = u_x(y)\hat{\boldsymbol{x}}$. In this stationary state, the Boltzmann equation (1) becomes

$$\left(-\frac{\zeta T}{2m}\frac{\partial^2}{\partial \boldsymbol{c}^2} - g\frac{\partial}{\partial c_x} + c_y\frac{\partial}{\partial y}\right) f = J[f, f]. \tag{13}$$

Here we focus on determining the solution to Eq. (13) in the bulk region of the channel which is sufficiently away from two walls such that the wall effects can be neglected. Note that the granular temperature (T) and the cooling rate (ζ, and hence the dependence on inelasticity) appear explicitly in Eq. (13) which must be simultaneously solved along with the hydrodynamic equations. In the steady state the balance equations for momentum and energy, Eq. (2), reduce to

$$\frac{dP_{yy}}{dy} = 0, \quad \frac{dP_{yx}}{dy} = -\rho g, \quad P_{yx}\frac{du_x}{dy} + \frac{dq_y}{dy} = 0. \tag{14}$$

The first equation of Eq. (14) implies that the normal stress P_{yy} is uniform throughout the system, and the second equation implies a linear dependence of the shear stress, $P_{yx} = -\rho g y$, on transverse distance (y). Clearly, the shear stress is generated due to the imposed gravitational acceleration, and so is the normal heat flux,

$$q_y = g\int y\rho(y)\frac{du_x}{dy}dy. \tag{15}$$

Since the local shear rate can be written as $du_x/dy = -P_{yx}/\eta \propto g$, where η is the shear viscosity of the gas, it follows from Eq. (15) that

$$q_y \propto g^2. \tag{16}$$

This implies that the normal heat flux is a quadratic order, $O(g^2)$, effect in gravity-driven Poiseuille flow, but the shear stress (or, the shear rate or velocity) is a linear order $O(g)$ effect.

B. BGK-like kinetic model for a heated granular gas

The mathematical difficulties with the Boltzmann equation are embodied in the collision operator $J[f, f]$ whose explicit form, with molecular chaos assumption, for a dilute granular gas is

$$J[f, f] = \sigma^2\int d\boldsymbol{c}_1\int d\hat{\boldsymbol{\sigma}}\,\mathcal{H}(\boldsymbol{c}_{01}\cdot\hat{\boldsymbol{\sigma}})(\boldsymbol{c}_{01}\cdot\hat{\boldsymbol{\sigma}}) \times\left[e_n^{-2}f(\boldsymbol{c}'')f(\boldsymbol{c}_1'') - f(\boldsymbol{c})f(\boldsymbol{c}_1)\right], \tag{17}$$

where $\mathcal{H}(\cdot)$ represents the Heaviside step function, and the double-primed velocities $(\boldsymbol{c}'', \boldsymbol{c}_1'')$ denote the precollisional velocities for the restituting or inverse collision which leads to $(\boldsymbol{c}, \boldsymbol{c}_1)$ following an inelastic binary collision. For the ease of analysis as well as to obtain explicit analytical results, researchers [24,29,37,38] have extended the well-studied Bhatnagar-Gross-Krook (BGK) kinetic model of molecular gases to inelastic or dissipative collisions. Following these pioneering works, the collision operator $J[f, f]$ is approximated by a BGK-like kinetic model [24,29]:

$$J[f, f] \to -\beta(e_n)\nu(f - f_M) + \frac{\zeta_M}{2}\frac{\partial}{\partial \boldsymbol{c}}\cdot[(\boldsymbol{c} - \boldsymbol{u})f], \tag{18}$$

where ν is the collision frequency [Eq. (11)], f_M is the local Maxwellian distribution [Eq. (9)], ζ_M is the cooling rate [Eq. (10)], and $\beta(e_n)$ is an unknown function of the restitution coefficient which must be chosen appropriately as described below. The first term on the right-hand side of Eq. (18) is an analog of the BGK model that describes a single-time collisional relaxation towards the local equilibrium with an "effective" collision frequency $\beta\nu$, and the second term describes the collisional cooling effects, which can be treated simply as an effective "drag" force that produces the same rate of energy loss as that yielded by the inelastic collisions [29]. Note that the kinetic model in Eq. (18) is a simplified version of the original formulation of Brey *et al.* [24] in that the exact local homogeneous cooling state of the Boltzmann equation is replaced by the local Maxwellian f_M [Eq. (9)] and the exact cooling rate ζ [Eq. (6)] is approximated by ζ_M [Eq. (10)].

The unknown function $\beta(e_n)$ in Eq. (18) is generally chosen to optimize the agreement between the kinetic-model description and the Boltzmann description. With a proper choice of $\beta(e_n)$, excellent quantitative agreement between the Boltzmann equation and the kinetic model (18) has been noted in the literature [21,24,29,37,38] for a variety of flow configurations. The Navier-Stokes (NS) transport coefficients [i.e., shear viscosity (η), thermal conductivity (κ), and Dufour coefficient (μ)] derived from the kinetic model (18) with white-noise forcing are given by [39]

$$\eta = \frac{p}{\beta\nu + \zeta_M}, \quad \kappa = \frac{5p}{2m\left(\beta\nu + \frac{3}{2}\zeta_M\right)}, \quad \mu = 0. \tag{19}$$

Note that the above quantities also depend on the kurtosis of the distribution function which is neglected in the present analysis. The choice for the dimensionless function $\beta(e_n)$, which makes the shear viscosity η [Eq. (19)] agree with its approximate Boltzmann result for a heated granular gas ($\eta_B = p/\nu_\eta$, with $\nu_\eta \approx (1 + e_n)(3 - e_n)\nu/4$ [40]), is

$$\beta(e_n) = \tfrac{1}{6}(1 + e_n)(2 + e_n). \tag{20}$$

Another choice for $\beta(e_n)$ can be made by matching the thermal conductivity κ with its Boltzmann value. For the present analysis, we will take $\beta(e_n)$ as given by Eq. (20).

With the aid of Eq. (18), the Boltzmann kinetic equation (13) to describe the stationary gravity-driven flow of a heated granular gas is modified to

$$\left(-g\frac{\partial}{\partial c_x} + c_y\frac{\partial}{\partial y}\right) f = -\beta\nu(f - f_M) + \frac{\zeta_M}{2}\frac{\partial}{\partial \boldsymbol{c}}\cdot\left(\boldsymbol{C} + \frac{T}{m}\frac{\partial}{\partial \boldsymbol{c}}\right) f. \tag{21}$$

Equation (21) must be solved in conjunction with related hydrodynamic balance equations (14) to yield solutions for hydrodynamic fields and fluxes for a heated granular gas under gravity; the boundary conditions are redundant since

we are interested in the bulk solution around the channel centerline [12,15,29].

III. SOLUTION FOR GRAVITY-DRIVEN POISEUILLE FLOW OF A HEATED GRANULAR GAS

Decomposing the nonequilibrium distribution function as

$$f = f_M(1+\Phi), \tag{22}$$

where Φ represents the deviation from the local Maxwellian distribution f_M, Eq. (21) becomes

$$\begin{aligned}(1+\Phi)&\left[C_y\widetilde{\partial}_y \ln f_M - \left(g + C_y\frac{\partial u_x}{\partial y}\right)\frac{\partial}{\partial C_x}\ln f_M\right]\\ &= \left(g + C_y\frac{\partial u_x}{\partial y}\right)\frac{\partial\Phi}{\partial C_x} - C_y\widetilde{\partial}_y\Phi - (\nu'-\zeta_M)\Phi\\ &\quad + \frac{\zeta_M}{2}\left[\left(\frac{T}{m}\frac{\partial}{\partial \boldsymbol{C}} - \boldsymbol{C}\right)\cdot\frac{\partial\Phi}{\partial \boldsymbol{C}}\right],\end{aligned} \tag{23}$$

where the operator $\widetilde{\partial}_y$ is defined via

$$\widetilde{\partial}_y \equiv \frac{\partial}{\partial y} + \left(\frac{\partial u_x}{\partial y}\right)\frac{\partial}{\partial C_x}, \tag{24}$$

and ν' is the modified collision frequency [29],

$$\nu' = \beta\nu + \zeta_M \equiv \nu\left[\beta(e_n) + \tfrac{5}{12}\left(1-e_n^2\right)\right], \tag{25}$$

which can be tied to the shear viscosity of a heated granular gas via Eq. (19).

The state at the channel centerline, i.e, the midpoint $y = 0$, is chosen as the reference state and the following dimensionless quantities are introduced:

$$\begin{aligned} y^* &= \frac{y\nu_0'}{c_0}, \quad \boldsymbol{C}^* = \frac{\boldsymbol{C}}{c_0}, \quad \boldsymbol{u}^* = \frac{\boldsymbol{u}}{c_0}, \quad f_M^* = \frac{f_M c_0^3}{n_0},\\ T^* &= \frac{T}{T_0}, \quad \nu'^* = \frac{\nu'}{\nu_0'}, \quad \boldsymbol{P}^* = \frac{\boldsymbol{P}}{p_0}, \quad \boldsymbol{q}^* = \frac{\boldsymbol{q}}{p_0 c_0},\end{aligned} \tag{26}$$

where the subscript 0 denotes quantities evaluated at $y = 0$; for example, $c_0 = \sqrt{2T_0/m}$ is the thermal velocity at the channel centreline $y = 0$. In Eq. (26), y^* measures distance in units of a nominal mean-free path, while

$$g^* = \frac{g}{\nu_0' c_0} \tag{27}$$

measures the strength of the gravity field acting on a particle that moves a distance of the mean-free path with the thermal velocity. The dimensionless version of Eq. (23) is

$$\begin{aligned}(1+\Phi)&\left[c_y^*\widetilde{\partial}_{y^*}\ln f_M^* + \frac{2(c_x^*-u_x^*)}{T^*}\left(g^* + c_y^*\frac{\partial u_x^*}{\partial y^*}\right)\right]\\ &= \left(g^* + c_y^*\frac{\partial u_x^*}{\partial y^*}\right)\frac{\partial\Phi}{\partial c_x^*} - c_y^*\widetilde{\partial}_{y^*}\Phi - \nu'^*(1-\zeta_0^*)\Phi\\ &\quad + \zeta_0^*\frac{\nu'^*}{2}\left[\left(\frac{T^*}{2}\frac{\partial}{\partial \boldsymbol{c}^*} - \boldsymbol{C}^*\right)\cdot\frac{\partial\Phi}{\partial \boldsymbol{c}^*}\right],\end{aligned} \tag{28}$$

where

$$\widetilde{\partial}_{y^*}\ln f_M^* = \frac{\partial \ln p^*}{\partial y^*} + \left(\frac{C^{*^2}}{T^*} - \frac{5}{2}\right)\frac{\partial \ln T^*}{\partial y^*}. \tag{29}$$

The cooling rate ζ_M in Eq. (28) has been rewritten in terms of the effective collision frequency ν' via $\zeta_M = \zeta_0^*\nu'$ [see Eqs. (10) and (25)], with

$$\zeta_0^* = \frac{\frac{5}{12}\left(1-e_n^2\right)}{\beta(e_n) + \frac{5}{12}\left(1-e_n^2\right)} \equiv \frac{5(1-e_n)}{2(2+e_n)+5(1-e_n)}, \tag{30}$$

and $\beta(e_n)$ is given by Eq. (20). In the remainder of this paper, the asterisks are omitted for convenience (e.g., $\zeta_0^* = \zeta_0$ and so on) and all quantities are understood to be expressed in dimensionless units. Note that the master kinetic equation [Eq. (28)] has been formulated in terms of particle velocity for ease of algebraic manipulation, following our previous work [15] on the gravity-driven Poiseuille flow of a molecular gas.

A. Perturbation expansion around channel centerline

Neglecting wall effects and focusing only on the bulk region of the channel around the centerline (Fig. 1), Eq. (28) is solved perturbatively by treating g^* as a small parameter [15,29]. The expansion of Φ in powers of gravitational acceleration g is

$$\Phi(\boldsymbol{c}; y, g) = \sum_{\alpha=1}^{n}\Phi^{(\alpha)}(\boldsymbol{c}; y)g^\alpha + O(g^{n+1}), \tag{31}$$

and we will present results up to $n = 4$ (i.e., fourth order in g).

In the absence of gravity, the solution of Eq. (21) is $f = f_M$ and $\Phi = 0$, with uniform density and temperature and zero velocity. The spatial dependence of hydrodynamic fields in the present problem of Poiseuille flow is a consequence of the gravitational acceleration and the shear stress at lateral walls. Due to the symmetry of the Poiseuille flow (Fig. 1), p and T are even functions of g, while u_x is an odd function of g. Therefore, the expansions for the hydrodynamic fields can be written as

$$p(y) = 1 + \sum_{\alpha=1}^{[n/2]} p^{(2\alpha)}(y)g^{2\alpha} + O(g^{2[n/2]+2}), \tag{32a}$$

$$T(y) = 1 + \sum_{\alpha=1}^{[n/2]} T^{(2\alpha)}(y)g^{2\alpha} + O(g^{2[n/2]+2}), \tag{32b}$$

$$u_x(y) = u_0 + \sum_{\alpha=1}^{[(n+1)/2]} u^{(2\alpha-1)}(y)g^{2\alpha-1} + O(g^{2[(n+1)/2]+1}), \tag{32c}$$

with the spatial dependence appearing via the coefficient functions $p^{(2\alpha)}(y)$, $T^{(2\alpha)}(y)$, and $u^{(2\alpha-1)}(y)$. Further it is assumed that $u_0 = 0$, which is equivalent to performing a Galilean transformation to a reference frame moving with the fluid at $y = 0$. Using Eqs. 32(a) and 32(b), the effective collision frequency for hard spheres, $\nu' = pT^{-1/2}$ [3,7], can be expressed in terms of g:

$$\begin{aligned}\nu' = 1 &+ \left(p^{(2)} - \frac{1}{2}T^{(2)}\right)g^2 + \left(p^{(4)} - \frac{p^{(2)}T^{(2)}}{2}\right.\\ &\left. + \frac{3}{8}T^{(2)^2} - \frac{T^{(4)}}{2}\right)g^4 + O(g^6).\end{aligned} \tag{33}$$

It can be verified that only $\nu' = 1$ is required in the evaluation of first- and second-order deviations $\Phi^{(1)}$ and $\Phi^{(2)}$, while $\nu' = 1 + (p^{(2)} - \frac{1}{2}T^{(2)})g^2$ is needed in the evaluation of the higher-order deviations $\Phi^{(3)}$ and $\Phi^{(4)}$ of the distribution function.

Substituting Eqs. (31), (32), and (33) into Eq. (28) and equating terms of the same order in g, we obtain the master kinetic equation at the kth order in $O(g^k)$:

$$(1 - \mathscr{A})\Phi^{(k)} \equiv \phi^{(k)}, \tag{34}$$

where the operator $\mathscr{A}$ is defined as

$$\mathscr{A} = \frac{\zeta_0}{2(1-\zeta_0)}\left[\left(\frac{1}{2}\frac{\partial}{\partial \boldsymbol{c}} - \boldsymbol{c}\right)\cdot\frac{\partial}{\partial \boldsymbol{c}}\right] - \frac{c_y}{1-\zeta_0}\frac{\partial}{\partial y}, \tag{35}$$

and the explicit expressions for the source term $\phi^{(k)}$, up to fourth order ($k = 4$), are given in Appendix A.

The solution to Eq. (34) can be written in operator form

$$\Phi^{(k)}(\boldsymbol{c}; y) = (1 - \mathscr{A})^{-1}\phi^{(k)} = \sum_{n=0}^{\infty} \mathscr{A}^n \phi^{(k)}. \tag{36}$$

Note that the source terms $\phi^{(k)}$ are functions of hydrodynamic fields at the same order which remain unknown. Based on the symmetries of Poiseuille-type flow, the unknown hydrodynamic profiles are guessed which, in turn, determines the functional form of the source term $\phi^{(k)}$. The latter helps to identify a trial form for the distribution function $\Phi^{(k)}(\boldsymbol{c}; y)$ with undetermined coefficients. The validity of guessed solutions and the unknown coefficients are then determined by satisfying the consistency conditions:

$$\int d\boldsymbol{C}\, f_M \Phi = 0, \quad \int d\boldsymbol{C} C_y f_M \Phi = 0, \tag{37a}$$

$$\int d\boldsymbol{C} C_x f_M \Phi = 0, \quad \int d\boldsymbol{C} C^2 f_M \Phi = 0, \tag{37b}$$

which follow from the definition of hydrodynamic fields.

B. Leading-order solutions: $O(g)$ and $O(g^2)$

The leading solution of this problem has been determined by Tij and Santos [29] which is briefly summarized in this section. At first order in g, Eq. (34) yields $(1 - \mathscr{A})\Phi^{(1)} = \phi^{(1)}$, with its source term being

$$\phi^{(1)} = -\frac{2}{1-\zeta_0}\left(c_x + c_x c_y \frac{\partial u^{(1)}}{\partial y}\right), \tag{38}$$

whose spatial dependence occurs via that of $du^{(1)}/dy$ which is unknown. From the Navier-Stokes solution for Poiseuille flow, the first-order velocity profile is assumed to be of parabolic shape:

$$u^{(1)}(y) = u_2^{(1)} y^2. \tag{39}$$

Putting Eqs. (38) and (39) into Eq. (36), it can be verified that the first-order distribution function $\Phi^{(1)}$ must have the following form:

$$\Phi^{(1)}(\boldsymbol{c}; y) = c_x\left(a_0 + a_1 c_y^2 + a_2 c_y y\right). \tag{40}$$

The unknown coefficients a_0, a_1, a_2 are obtained by inserting Eq. (40) into $(1 - \mathscr{A})\Phi^{(1)} = \phi^{(1)}$, yielding

$$a_0 = \frac{4\left(-2 - \zeta_0 + 2u_2^{(1)}\zeta_0\right)}{(4 - {\zeta_0}^2)}, \quad a_1 = \frac{8u_2^{(1)}}{2+\zeta_0}, \quad a_2 = -4u_2^{(1)}, \tag{41}$$

and the third consistency condition of Eqs. (37) gives $u_2^{(1)} = 1$, and therefore both $u^{(1)}(y)$ and $\Phi^{(1)}(\boldsymbol{c}; y)$ are completely determined. Inserting the explicit form of $\Phi^{(1)}$ in Eqs. (4) and (5), the nonzero components of the fluxes, to first order in g, are found to be

$$P_{yx}^{(1)}(y) = -2y \quad \text{and} \quad q_x^{(1)}(y) = \frac{2}{2+\zeta_0}. \tag{42}$$

At second order $O(g^2)$, the source term $\phi^{(2)}$ in Eq. (34) [see Eq. (A1) in Appendix A] depends on two hydrodynamic fields: pressure $p^{(2)}$ and temperature $T^{(2)}$, which are even functions of y in a Poiseuille-type flow. The latter two unknown quantities are assumed to be of the form

$$p^{(2)}(y) = p_2^{(2)} y^2 \quad \text{and} \quad T^{(2)}(y) = \sum_{\alpha=1,2} T_{2\alpha}^{(2)} y^{2\alpha}. \tag{43}$$

A trial solution for the second-order distribution function $\Phi^{(2)}$ is assumed [see Eq. (A4) in Appendix A], with its unknown coefficients b_i being expressed in terms of $p_2^{(2)}$, $T_2^{(2)}$, and $T_4^{(2)}$; Sec. I of the Supplemental Material [41] contains the expressions of the coefficients b_i as functions of ζ_0. At this order, the third consistency condition of Eq. (37) holds due to symmetry, while the second consistency condition is identically fulfilled irrespective of the values of $p_2^{(2)}$, $T_2^{(2)}$, and $T_4^{(2)}$; the remaining two consistency conditions yield

$$T_2^{(2)} = \frac{4\left(38 + 43\zeta_0 + 17\zeta_0^2\right)}{25(1+\zeta_0)(2+\zeta_0)}, \tag{44a}$$

$$T_4^{(2)} = -\frac{2}{15}(2+\zeta_0), \quad p_2^{(2)} = \frac{24}{5}, \tag{44b}$$

and hence the second-order corrections to hydrodynamic profiles Eq. (43) as well as the explicit form of $\Phi^{(2)}(\boldsymbol{c}; y)$ are determined. The latter is used to calculate the second-order contributions to the fluxes:

$$P_{xx}^{(2)} = \frac{32\left(82 + 67\zeta_0 + 8\zeta_0^2\right)}{25(1+\zeta_0)(2+\zeta_0)^2} + \frac{56}{5}y^2, \tag{45a}$$

$$P_{yy}^{(2)} = -\frac{24\left(102 + 87\zeta_0 + 13\zeta_0^2\right)}{25(1+\zeta_0)(2+\zeta_0)^2}, \tag{45b}$$

$$q_y^{(2)} = \frac{4}{3}y^3, \quad P_{xy}^{(2)} = 0 = q_x^{(2)}. \tag{45c}$$

The leading-order contributions to hydrodynamic [Eqs. (39), (43), and (44)] and flux profiles [Eqs. (42) and (45)] match those obtained by Tij and Santos [29] up to second order, although there seems to be printing mistakes in their Eqs. (3.24) and (3.31). In the limit of elastic collisions ($e_n = 1$), these solutions boil down to those for a molecular gas of elastic hard spheres [15] undergoing

acceleration-driven Poiseuille flow. One interesting point to note in Eqs. (42) and (45) is that while the normal heat flux appears at quadratic order $O(g^2)$ as discussed previously in Eq. (16), the tangential heat flux appears at linear order $O(g)$ which is known to be a Burnett-order effect in the standard Chapman-Enskog expansion [3]. The latter finding makes the connection of the g-based perturbation expansion with the standard Chapman-Enskog expansion subtle; this issue will be discussed in Sec. VII.

C. Higher-order solutions: $O(g^3)$ and $O(g^4)$

To solve the third-order $[O(g^3)]$ equation $(1-\mathscr{A})\Phi^{(3)} = \phi^{(3)}$, it is to be noted that its source term contains a third-order quantity $du^{(3)}/dy$ [see Eq. (A2)] which is unknown at this order. The third-order velocity profile is taken to be

$$u^{(3)}(y) = \sum_{\alpha=1}^{3} u_{2\alpha}^{(3)} y^{2\alpha} \tag{46}$$

and the structure of $\mathscr{A}^n\phi^{(3)}$ [viz., Eq. (36)] suggests a trial distribution function of the form

$$\begin{aligned}
&\Phi^{(3)}(y,\boldsymbol{c}) \\
&= c_x\big[c_0c_y^8 + c_1c_x^2 + c_2 + c_y^6\big(c_4c_x^2 + c_5\big) \\
&\quad + c_z^2\big(c_6c_y^6 + c_7c_y^2 + c_8c_y^4 + c_9\big) + c_y^2\big(c_{10}c_x^2 + c_{11}\big) \\
&\quad + c_y^4\big(c_{12}c_x^2 + c_{13}\big) + y\big\{c_{24}c_y^7 + c_y^3\big(c_{25}c_x^2 + c_{26}\big) \\
&\quad + c_z^2\big(c_{27}c_y^5 + c_{28}c_y + c_{29}c_y^3\big) + c_y^5\big(c_{30}c_x^2 + c_{31}\big) \\
&\quad + c_y\big(c_{32}c_x^2 + c_{33}\big)\big\} + y^2\big\{c_{14}c_y^6 + c_{15} + c_{16}c_x^2 \\
&\quad + c_y^4\big(c_{17}c_x^2 + c_{18}\big) + c_z^2\big(c_{19}c_y^4 + c_{20}c_y^2 + c_{21}\big) \\
&\quad + c_y^2\big(c_{22}c_x^2 + c_{23}\big)\big\} + y^3\big\{c_{34}c_y^5 + c_z^2\big(c_{35}c_y + c_{36}c_y^3\big) \\
&\quad + c_y^3\big(c_{37}c_x^2 + c_{38}\big) + c_y\big(c_{39}c_x^2 + c_{40}\big)\big\} \\
&\quad + y^4\big\{c_{41}c_y^4 + c_{42}c_x^2 + c_{43} + c_z^2\big(c_{44}c_x^2 + c_{45}\big) \\
&\quad + c_z^2\big(c_{46}c_y^2 + c_{47}\big)\big\} + c_3c_y y^5\big].
\end{aligned} \tag{47}$$

The above unknown coefficients c_i can be expressed in terms of $u_{2\alpha}^{(3)}$ by inserting Eq. (47) into $(1-\mathscr{A})\Phi^{(3)} = \phi^{(3)}$ as given in Sec. II of the Supplemental Material [41].

Using consistency conditions Eq. (37), the coefficients $u_{2\alpha}^{(3)}$ in Eq. (46) are found to be

$$u_2^{(3)} = \frac{16\beta_1(\zeta_0)}{25(1+\zeta_0)^2(2+\zeta_0)^3(2+3\zeta_0)}, \tag{48a}$$

$$u_4^{(3)} = \frac{1}{15}\left(83 - \frac{12}{1+\zeta_0} + \frac{116}{2+\zeta_0}\right), \tag{48b}$$

$$u_6^{(3)} = \frac{7(2+\zeta_0)}{225}, \tag{48c}$$

with the expression for $\beta_1(\zeta_0)$ being given in Appendix A 1, and the third-order contribution to hydrodynamic profiles is thus determined. By substituting these values into the expressions of the coefficients c_i, we obtain the explicit expression for $\Phi^{(3)}(\boldsymbol{c}; y)$ which helps to determine third-order contributions to the flux terms:

$$P_{yx}^{(3)} = -\frac{4\big[44 + 94\zeta_0 + 26\zeta_0^2 + y^2(1+\zeta_0)(2+\zeta_0)^2\big]y^3}{75(1+\zeta_0)(2+\zeta_0)}, \tag{49a}$$

$$P_{xx}^{(3)} = 0 = P_{yy}^{(3)} = q_y^{(3)}, \tag{49b}$$

$$\begin{aligned}
q_x^{(3)} &= -\frac{2\big(114 + 257\zeta_0 + 58\zeta_0^2\big)y^4}{15(2+\zeta_0)(1+2\zeta_0)} \\
&\quad - \frac{4\mathcal{C}_1(\zeta_0)}{25}[\beta_3(\zeta_0)y^2 + 2\beta_2(\zeta_0)],
\end{aligned} \tag{49c}$$

where $\mathcal{C}_1(\zeta_0) = 1/(1+\zeta_0)^3(2+\zeta_0)^4(1+2\zeta_0)(2+3\zeta_0)^2$ and the expressions for $\beta_2(\zeta_0)$ and $\beta_3(\zeta_0)$ are given in Appendix A 1.

To solve Eq. (34) at fourth order $O(g^4)$, the pressure and temperature profiles are taken to be

$$p^{(4)}(y) = \sum_{\alpha=1}^{3} p_{2\alpha}^{(4)} y^{2\alpha} \quad \text{and} \quad T^{(4)}(y) = \sum_{\alpha=1}^{4} T_{2\alpha}^{(4)} y^{2\alpha}. \tag{50}$$

The structure of $\mathscr{A}^n\phi^{(4)}$ suggests a trial distribution function of the form $\Phi^{(4)}(y,\boldsymbol{c}) = d_0c_y^{12} + d_1c_x^4 + \cdots$ [see Eq. (A5)]. This along with Eq. (50) helps to solve $(1-\mathscr{A})\Phi^{(4)} = \phi^{(4)}$, yielding expressions for unknown coefficients d_i of $\Phi^{(4)}$ in terms of $p_2^{(4)}$, $p_4^{(4)}$, $p_6^{(4)}$, $T_2^{(4)}$, $T_4^{(4)}$, $T_6^{(4)}$, and $T_8^{(4)}$; the detailed expressions of d_i as functions of ζ_0 are presented in Sec. III of the Supplemental Material [41].

By satisfying Eq. (37), the expressions of $p_j^{(4)}$ and $T_j^{(4)}$ are found as

$$p_2^{(4)} = -\frac{96\mathcal{C}_1(\zeta_0)\beta_4(\zeta_0)}{625}, \quad p_6^{(4)} = \frac{32(2+\zeta_0)}{125}, \tag{51a}$$

$$p_4^{(4)} = \frac{-32\big(1876 + 1704\zeta_0 + 127\zeta_0^2 - 53\zeta_0^3\big)}{125(1+\zeta_0)(2+\zeta_0)^2}, \tag{51b}$$

$$T_2^{(4)} = -\frac{32\mathcal{C}_2(\zeta_0)\beta_5(\zeta_0)}{3125}, \quad T_8^{(4)} = -\frac{62(2+\zeta_0)^2}{7875}, \tag{51c}$$

$$T_4^{(4)} = -\frac{8(2+\zeta_0)\mathcal{C}_1(\zeta_0)\beta_6(\zeta_0)}{1875}, \tag{51d}$$

$$T_6^{(4)} = -\frac{8\big(8692 + 11868\zeta_0 + 5579\zeta_0^2 + 759\zeta_0^3\big)}{5625(1+\zeta_0)(2+\zeta_0)}, \tag{51e}$$

where $\mathcal{C}_2(\zeta_0) = \mathcal{C}_1(\zeta_0)/(1+\zeta_0)(1+2\zeta_0)(2+3\zeta_0)(2+5\zeta_0)$. Subsequently, the fourth-order contributions to the fluxes are determined using the exact form of $\Phi^{(4)}$:

$$\begin{aligned}
P_{xx}^{(4)} &= \frac{224}{375}(2+\zeta_0)y^6 - \frac{32\beta_7(\zeta_0)y^4}{375} \\
&\quad - \frac{32\beta_8(\zeta_0)\mathcal{C}_2(\zeta_0)}{625(2+\zeta_0)}y^2 - \frac{512\beta_9(\zeta_0)\mathcal{C}_2(\zeta_0)}{3125(2+\zeta_0)},
\end{aligned} \tag{52a}$$

$$P_{yy}^{(4)} = \frac{384\beta_{10}(\zeta_0)\mathcal{C}_2(\zeta_0)}{3125(2+\zeta_0)}, \tag{52b}$$

$$q_y^{(4)} = \frac{12}{175}(2+\zeta_0)y^7 + \frac{8\beta_{11}(\zeta_0)y^5}{375} + \frac{64\beta_{12}(\zeta_0)y^3}{75}, \tag{52c}$$

and the expressions for $\beta_4(\zeta_0)$ to $\beta_{12}(\zeta_0)$ are given in Appendix A 1. The remaining flux terms ($P_{xy}^{(4)} = 0 = q_x^{(4)}$) are zero at this order.

D. Structure of hydrodynamic and flux fields at each order in g

At each order $O(g^\alpha)$, it is straightforward to verify that the spatial structures of the hydrodynamic profiles [Eqs. (39), (43), (46), (50)] and the associated flux profiles [Eqs. (42), (45), (49), (52)] have the following polynomial representations:

$$\begin{aligned} u^{(2i-1)}(y) &= y^2\mathcal{P}_{2i-2}(y^2), \quad T^{(2i)}(y) = y^2\mathcal{P}_{2i-1}(y^2), \\ p^{(2i)}(y) &= y^2\mathcal{P}_{2i-2}(y^2), \quad P_{yx}^{(2i-1)}(y) = y^3\mathcal{P}_{2i-3}(y^2), \\ P_{yy}^{(2i)}(y) &= \text{const.}, \quad P_{xx}^{(2i)}(y) = \mathcal{P}_{2i-1}(y^2), \\ q_x^{(2i-1)}(y) &= \mathcal{P}_{2i-2}(y^2), \quad q_y^{(2i)}(y) = y^3\mathcal{P}_{2i-2}(y^2), \end{aligned} \tag{53}$$

where $\mathcal{P}_j(y^2)$ denotes an arbitrary polynomial of degree j in y^2.

Combining solutions up to fourth order [Eqs. (39), (43), (46), (50)], the expressions for each hydrodynamic field are found which in real units read as

$$u_x(y) = \underline{u_0 + \left(\frac{\rho_0 g}{2\eta_0}\right)y^2} + u_2^{(3)}\left(\frac{m^3\eta_0 g^3}{4\rho_0 T_0^3}\right)y^2 + u_4^{(3)}\left(\frac{m^2\rho_0 g^3}{8\eta_0 T_0^2}\right)y^4 + u_6^{(3)}\left(\frac{m\rho_0^3 g^3}{16\eta_0^3 T_0}\right)y^6 + O(g^5), \tag{54}$$

$$T(y) = T_0\Bigg[\underline{1 + T_4^{(2)}\left(\frac{m\rho_0^2 g^2}{8\eta_0^2 T_0}\right)y^4 + T_2^{(2)}\left(\frac{mg}{2T_0}\right)^2 y^2} + T_2^{(4)}\left(\frac{m^5\eta_0^2 g^4}{8\rho_0^2 T_0^5}\right)y^2 + T_4^{(4)}\left(\frac{mg}{2T_0}\right)^4 y^4 + T_6^{(4)}\left(\frac{m^3\rho_0^2 g^4}{32\eta_0^2 T_0^3}\right)y^6 + T_8^{(4)}\left(\frac{m^2\rho_0^4 g^4}{64\eta_0^4 T_0^2}\right)y^8\Bigg] + O(g^6), \tag{55}$$

$$p(y) = p_0\Bigg[\underline{1 + p_2^{(2)}\left(\frac{mg}{2T_0}\right)^2 y^2} + p_2^{(4)}\left(\frac{m^5\eta_0^2 g^4}{8\rho_0^2 T_0^5}\right)y^2 + p_4^{(4)}\left(\frac{mg}{2T_0}\right)^4 y^4 + p_6^{(4)}\left(\frac{m^3\rho_0^2 g^4}{32\eta_0^2 T_0^3}\right)y^6\Bigg] + O(g^6), \tag{56}$$

$$\rho(y) = \frac{mp(y)}{T(y)}. \tag{57}$$

The underlined terms in each expression correspond to results up to "second order" in the gravitational acceleration, and the remaining terms are fourth order. Similarly, adding Eqs. (42), (45), (49), and (52), the fourth-order solutions for flux terms ($P_{\alpha\beta}$ and q_α) are obtained which are discussed in Sec. V.

IV. HYDRODYNAMICS: RAREFACTION EFFECTS ON TEMPERATURE AND THE ROLE OF INELASTICITY

In order to explore the temperature field in detail, we scale the y coordinate in terms of the centerline mean-free path, $\lambda_0 = (\pi\sqrt{2}n_0\sigma^2)^{-1} \equiv (8/5\sqrt{\pi})(c_0/\nu_0)$, which is defined as the average distance traveled by a molecule or particle between two successive collisions. Let us introduce the "local" Froude number ($\mathrm{Fr} = g\lambda/c^2$), defined as the ratio of gravitational and inertial forces, and it measures the influence of gravity on the flow field. The Froude number at the channel centerline is given by

$$\mathrm{Fr}_0 = \frac{g\lambda_0}{c_0^2} \equiv \frac{8}{5\sqrt{\pi}}\frac{(3-e_n)(1+e_n)}{4}g^*, \tag{58}$$

which depends on the restitution coefficient and the dimensionless gravitational acceleration g^* [Eq. (27)].

In terms of the centerline Froude number (58) and the rescaled transverse coordinate y/λ_0, the temperature profile (55) can be rewritten as

$$\frac{T(y)}{T_0} = \underline{1 + \mathrm{Fr}_0^2\sum_{\alpha=1}^{2} A_T^{(2\alpha)}(e_n)\left(\frac{y}{\lambda_0}\right)^{2\alpha}} + \mathrm{Fr}_0^4\sum_{\alpha=1}^{4} B_T^{(2\alpha)}(e_n)\left(\frac{y}{\lambda_0}\right)^{2\alpha} + O\left(\mathrm{Fr}_0^6\right), \tag{59}$$

where the inelasticity-dependent coefficients are given by

$$A_T^{(2)}(e_n) = \frac{4\left(2719 - 2741e_n + 706e_n^2\right)}{25(7-4e_n)(23-11e_n)} > 0, \tag{60a}$$

$$A_T^{(4)}(e_n) = -\frac{8(3-e_n)(1+e_n)^2(23-11e_n)}{1125\pi} < 0, \tag{60b}$$

$$B_T^{(2)}(e_n) = \frac{25\pi}{4\left(3+2e_n-e_n^2\right)^2}\Bigg(-\frac{33267022075095579}{46981321887500} + \frac{511377408}{169(19-13e_n)^2} - \frac{497664000}{14641(23-11e_n)^4} + \frac{2189749248}{73205(23-11e_n)^2} - \frac{15390720}{49(11-7e_n)^2} - \frac{23085}{(7-4e_n)^4} - \frac{50053887}{100(7-4e_n)^2} - \frac{20977461}{100(7-4e_n)^3} - \frac{2127452263}{2500(7-4e_n)} - \frac{3686400}{49(11-7e_n)^3} + \frac{928213632}{875(11-7e_n)} + \frac{648843264}{14641(23-11e_n)^3} - \frac{1566633408}{1830125(23-11e_n)} + \frac{127918424064}{21125(19-13e_n)} - \frac{392000000}{31(43-31e_n)}\Bigg), \tag{60c}$$

$$B_T^{(4)}(e_n) = -\frac{247750795519}{3179426250} - \frac{1060608}{1331(23-11e_n)^2} + \frac{102400}{49(11-7e_n)^2} + \frac{96183}{50(7-4e_n)^2} + \frac{405}{2(7-4e_n)^3} + \frac{750619}{250(7-4e_n)} - \frac{776448}{1225(11-7e_n)} + \frac{829440}{1331(23-11e_n)^3} - \frac{635968}{33275(23-11e_n)} - \frac{700416}{65(19-13e_n)}, \tag{60d}$$

$$B_T^{(6)}(e_n) = -\frac{32(3-e_n)(1+e_n)^2\left(2082193-2926828e_n+1371221e_n^2-213674e_n^3\right)}{140625\left(161-169e_n+44e_n^2\right)\pi}, \tag{60e}$$

$$B_T^{(8)}(e_n) = -\frac{992(23-11e_n)^2(3-e_n)^2(1+e_n)^4}{44296875\pi^2}. \tag{60f}$$

In the remaining part of this section, we analyze the characteristics of the temperature profile and make a comparison between the second-order solution [i.e., underlined terms in Eq. (59)] and its fourth-order counterpart.

A. Temperature bimodality: Competition between rarefaction and inelasticity

Figure 2 compares the temperature profiles [T/T_0, Eq. (59)] for a molecular gas ($e_n = 1$) with those for dissipative gas ($e_n = 0.2$ and $e_n = 0.5$) at Froude numbers of (a) $\mathrm{Fr}_0 = 10^{-3}$ and (b) $\mathrm{Fr}_0 = 5 \times 10^{-3}$. It is seen that, for both molecular and granular gases, the temperature profile is of bimodal shape, with a local minimum at the channel centerline ($y = 0$) and two symmetric maxima ($T = T_{\max}$) away from the channel centerline (at $y = y_{\max}$); the overall shape of the temperature profile remains the same with the second-order solution too [i.e., retaining only the underlined terms in Eq. (59)]. It is evident from panel (b) ($\mathrm{Fr}_0 = 5 \times 10^{-3}$) that while the value of $T_{\max}$ increases with decreasing e_n, its transverse location $y_{\max}$ shifts away from $y = 0$ in the same limit. On the other hand, at lower values of $\mathrm{Fr}_0 = 10^{-3}$ [panel (a)], the dependencies of $T_{\max}$ and $y_{\max}$ on the restitution coefficient seem to be nonmonotonic as confirmed in the following analysis.

The transverse location $y_{\max}$ of two symmetric temperature maxima can be obtained by solving $dT/dy = 0$, yielding

$$\left(\frac{y_{\max}}{\lambda_0}\right)^2 = -\frac{A_T^{(2)}}{2A_T^{(4)}} + \frac{\left(-4{A_T^{(4)}}^3 B_T^{(2)} + 4A_T^{(2)}{A_T^{(4)}}^2 B_T^{(4)} - 3{A_T^{(2)}}^2 A_T^{(4)} B_T^{(6)} + 2{A_T^{(2)}}^3 B_T^{(8)}\right)\mathrm{Fr}_0^2}{8{A_T^{(4)}}^4} + \frac{\left(2{A_T^{(4)}}^2 B_T^{(4)} - 3A_T^{(2)}A_T^{(4)}B_T^{(6)} + 3{A_T^{(2)}}^2 B_T^{(8)}\right)\left(4{A_T^{(4)}}^3 B_T^{(2)} - 4A_T^{(2)}{A_T^{(4)}}^2 B_T^{(4)} + 3{A_T^{(2)}}^2 A_T^{(4)} B_T^{(6)} - 2{A_T^{(2)}}^3 B_T^{(8)}\right)\mathrm{Fr}_0^4}{16{A_T^{(4)}}^7} + O\left(\mathrm{Fr}_0^6\right). \tag{61}$$

Substituting this into Eq. (59), the expression for $T_{\max}$ can be obtained. To quantify the degree of temperature bimodality, we define the following quantity $\Delta T = (T_{\max} - T_0)/T_0$, dubbed *excess temperature*, which measures the relative value of the maximum temperature with respect to its centerline value. The expression for the excess temperature is given by

$$\Delta T = -\frac{{A_T^{(2)}}^2}{4A_T^{(4)}}\mathrm{Fr}_0^2 + \frac{A_T^{(2)}\left(-8{A_T^{(4)}}^3 B_T^{(2)} + 4A_T^{(2)}{A_T^{(4)}}^2 B_T^{(4)} - 2{A_T^{(2)}}^2 A_T^{(4)} B_T^{(6)} + {A_T^{(2)}}^3 B_T^{(8)}\right)}{16{A_T^{(4)}}^4}\mathrm{Fr}_0^4 + O\left(\mathrm{Fr}_0^6\right). \tag{62}$$

Typical variations of ΔT with restitution coefficient e_n are displayed in Fig. 3(a) for two values of $\mathrm{Fr}_0 = 10^{-3}$ (main panel) and $\mathrm{Fr}_0 = 5 \times 10^{-3}$ (inset); it is seen that ΔT is a nonmonotonic and monotonic function of e_n at smaller and larger values of Froude number. The latter transition is clearly evident in Fig. 3(b) which shows the variations of ΔT with Fr_0 for different e_n; in particular, there is a minimum or critical value of $\mathrm{Fr}_0^c = \mathrm{Fr}_0(e_n)$, above and below which the excess temperature monotonically increases and becomes nonmonotonic, respectively. The corresponding variations of the transverse location $y_{\max}$ [Eq. (61)] with (c) restitution coefficient e_n and (d) Froude number Fr_0 are displayed in Figs. 3(c) and 3(d). It is clear that the dependence of $y_{\max}$ on e_n follows a nonmonotonic and monotonic trend, similar to that of $T_{\max}$, at smaller and higher values of Froude number, respectively.

B. Comparison with second-order solution and the critical Froude number

All results presented in Fig. 3 are based on the fourth-order solution in Froude number $O(\mathrm{Fr}_0^4)$. The corresponding second-order solutions [$O(\mathrm{Fr}_0^2)$] for ΔT and $y_{\max}$ can be easily obtained by setting all third- and fourth-order terms to zero (i.e., $B_T^{(j)} = 0$) in Eqs. (61) and (62), yielding the solution of Tij and Santos [29],

$$\left(\frac{y_{\max}}{\lambda_0}\right)_{\mathrm{II}} = \pm\sqrt{-\frac{A_T^{(2)}(e_n)}{2A_T^{(4)}(e_n)}}, \tag{63}$$

and the rescaled excess temperature

$$\left(\frac{\Delta T}{\mathrm{Fr}_0^2}\right)_{\mathrm{II}} = -\frac{{A_T^{(2)}}^2(e_n)}{4A_T^{(4)}(e_n)}. \tag{64}$$

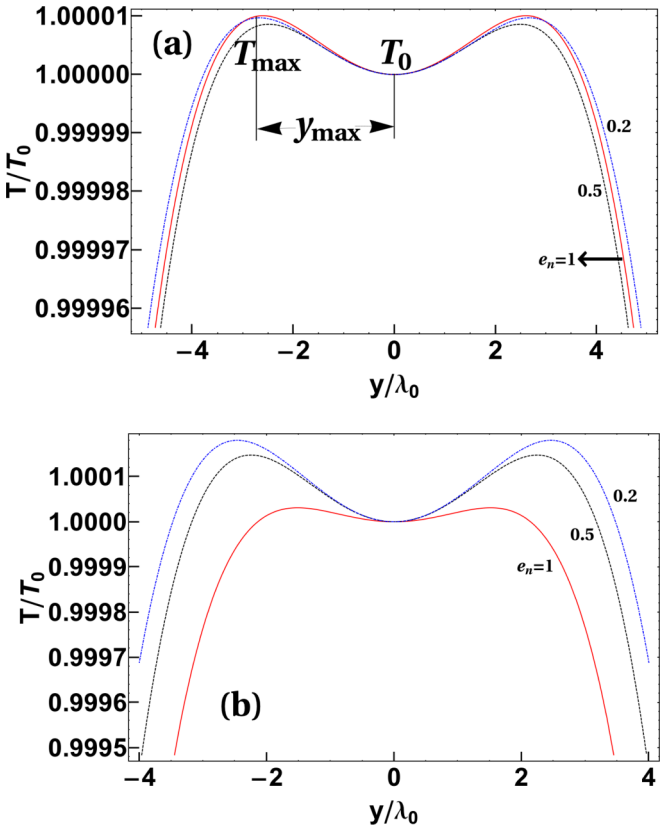

FIG. 2. Temperature profiles for (a) $\mathrm{Fr}_0 = 10^{-3}$ and (b) $\mathrm{Fr}_0 = 5 \times 10^{-3}$ with $e_n = 1$ (red solid line), $e_n = 0.5$ (black dashed line), and $e_n = 0.2$ [blue dot-dashed (top) line], as predicted by the kinetic model up to "fourth order" in g.

Both these quantities depend nonmonotonically on the restitution coefficient at any value of the Froude number as confirmed in Fig. 4, which is in contrast to the corresponding monotonic variations of their fourth-order solutions at larger values of $\mathrm{Fr}_0 > \mathrm{Fr}_0^c$. Moreover, the second-order solution for the excess temperature in Eq. (64) has a quadratic dependence on the Froude number, but its transverse location $(y_{\max})_{\mathrm{II}}$ is independent of Fr_0. It must be noted that these second-order results are in contrast to recent MD and DSMC results [31,32] that confirmed a monotonic increase of the excess temperature ΔT with decreasing e_n at any value of Fr_0. The latter simulations however do not contain the bulk heating via white noise that makes a direct one-to-one comparison of the present theoretical results with simulations [31,32] difficult; this issue is further discussed in Sec. VI B.

Based on the present higher-order solution, the transition from the "nonmonotonic" to "monotonic" dependence of the excess temperature ΔT on the restitution coefficient as a function of Froude number Fr_0 is illustrated in Fig. 5: while the panel (a) shows the contours of ΔT in the $(\mathrm{Fr}_0, 1 - e_n)$ plane, the panel (b) displays the corresponding contours of $d\Delta T/de_n$. The light yellow colored region around the lower left corner of Fig. 5(b) corresponds to $d\Delta T/de_n > 0$, implying that ΔT decreases with increasing dissipation in this region; in the remaining part of the phase diagram $d\Delta T/de_n < 0$, indicating ΔT increases with increasing dissipation. The

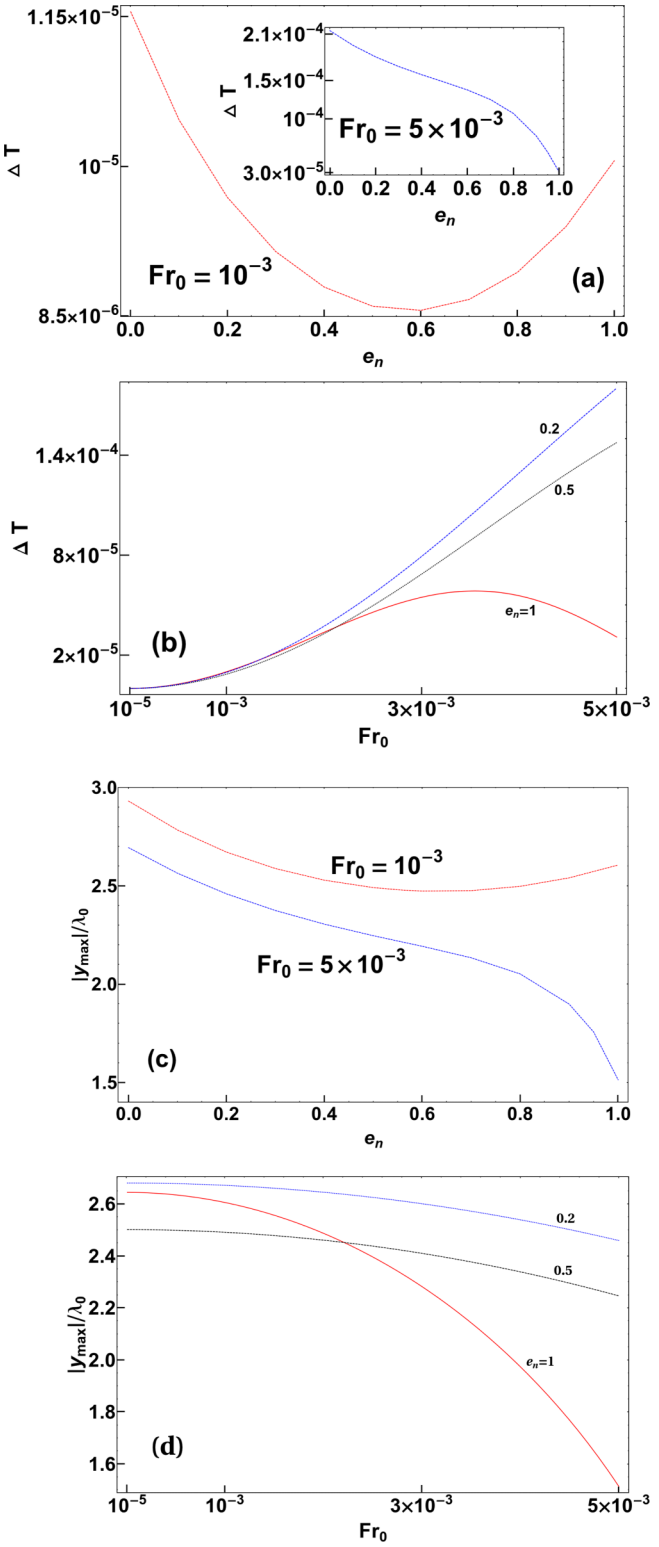

FIG. 3. (a) Variations of ΔT [Eq. (62)] with e_n for Froude numbers of $\mathrm{Fr}_0 = 10^{-3}$ (main panel) and $\mathrm{Fr}_0 = 5 \times 10^{-3}$ (inset); (b) variations of ΔT with Fr_0 for different values of the restitution coefficient: $e_n = 1$, bottom red line; $e_n = 0.5$, middle black line; $e_n = 0.2$, top blue line. (c), (d) Variations of $|y_{\max}|/\lambda_0$ [Eq. (61)] with (c) restitution coefficient e_n and (d) Froude number Fr_0.

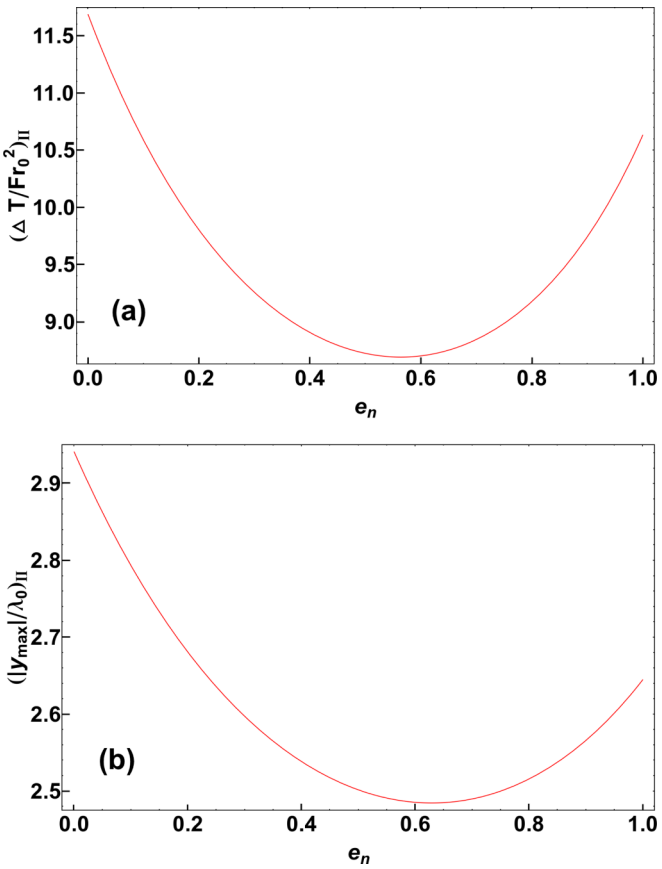

FIG. 4. Second-order solution for (a) rescaled excess temperature $(\Delta T/\mathrm{Fr}_0^2)_{\mathrm{II}}$ [as given in Eq. (64)] and (b) its transverse location $(|y_{\max}|/\lambda_0)_{\mathrm{II}}$ [Eq. (63)].

contour separating these two regions ($d\Delta T/de_n < 0$ and $d\Delta T/de_n > 0$) is denoted by

$$\mathrm{Fr}_0(e_n) = \mathrm{Fr}_0\left(\frac{d\Delta T}{de_n} = 0\right), \tag{65}$$

which depends on the restitution coefficient. Overall, Fig. 5(b) confirms that there is a critical Froude number

$$\mathrm{Fr}_0^c[\Delta T] \equiv \sup_{e_n} \mathrm{Fr}_0(e_n), \tag{66}$$

below which ΔT varies nonmonotonically with e_n but ΔT increases monotonically with increasing dissipation at $\mathrm{Fr}_0 > \mathrm{Fr}_0^c$. In other words, the inelasticity plays a "dual" role of increasing and decreasing ΔT at $\mathrm{Fr}_0 > \mathrm{Fr}_0^c$ and $\mathrm{Fr}_0 < \mathrm{Fr}_0^c$, respectively. These conclusions hold also for the related variations of the transverse location $y_{\max}$ of temperature maxima with inelasticity.

V. RHEOLOGY: PRESSURE TENSOR, HEAT FLUX, AND TRANSPORT COEFFICIENTS

A. Pressure tensor: Normal-stress differences and shear viscosity

The elements of the pressure tensor and the components of the heat flux up to fourth order in g have been determined in Secs. III B and III C. In real units, the diagonal components of

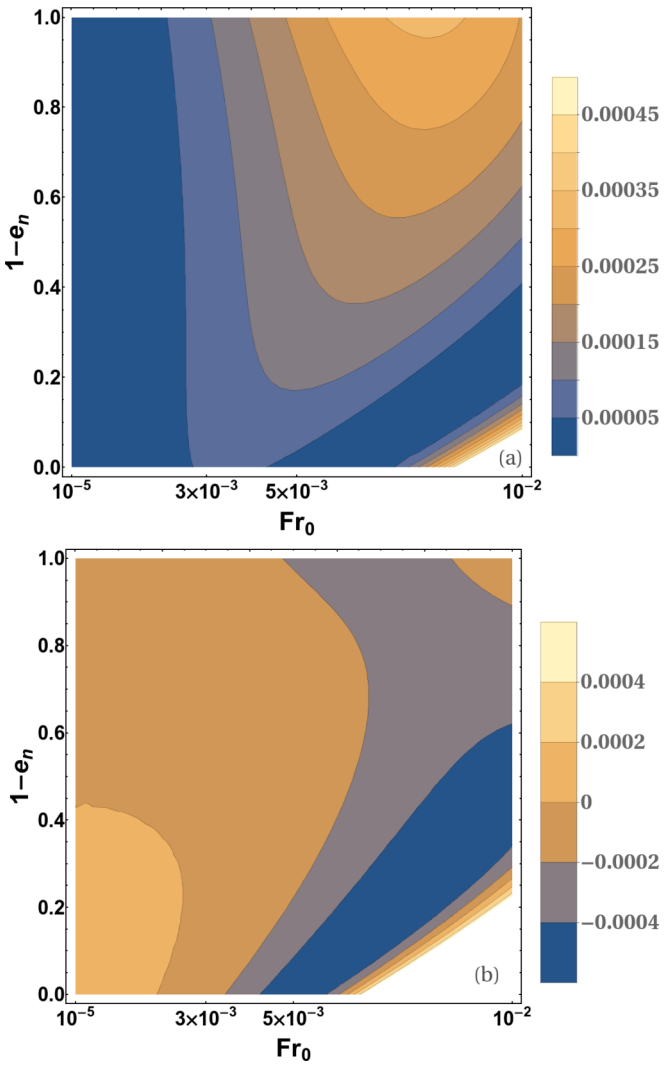

FIG. 5. Contour plots of (a) excess temperature ΔT [Eq. (62)] and (b) its derivative $d\Delta T/de_n$ in the $(\mathrm{Fr}_0, 1-e_n)$ plane. Note that $d\Delta T/de_n > 0$ around the left corner (light yellow-shaded region) of panel (b), and negative elsewhere.

the pressure tensor are given in terms of the centerline mean-free path (λ_0) and Froude number (Fr_0) as follows:

$$\frac{P_{xx}(y)}{p_0} = \underline{1 + \mathrm{Fr}_0^2 \sum_{\alpha=0}^{1} A_{P_{xx}}^{(2\alpha)} \left(\frac{y}{\lambda_0}\right)^{2\alpha}} + \mathrm{Fr}_0^4 \sum_{\alpha=0}^{3} B_{P_{xx}}^{(2\alpha)} \left(\frac{y}{\lambda_0}\right)^{2\alpha} + O\left(\mathrm{Fr}_0^6\right), \tag{67}$$

$$\frac{P_{yy}(y)}{p_0} = \underline{1 + \mathrm{Fr}_0^2\, A_{P_{yy}}^{(0)}} + \mathrm{Fr}_0^4\, B_{P_{yy}}^{(0)} + O\left(\mathrm{Fr}_0^6\right), \tag{68}$$

$$P_{zz} = 3p - P_{xx} - P_{yy}, \tag{69}$$

with the mean pressure having the following expression:

$$\frac{p(y)}{p_0} = \underline{1 + \mathrm{Fr}_0^2 A_p^{(2)} \left(\frac{y}{\lambda_0}\right)^2} + \mathrm{Fr}_0^4 \sum_{\alpha=1}^{3} B_p^{(2\alpha)} \left(\frac{y}{\lambda_0}\right)^{2\alpha} + O\left(\mathrm{Fr}_0^6\right), \tag{70}$$

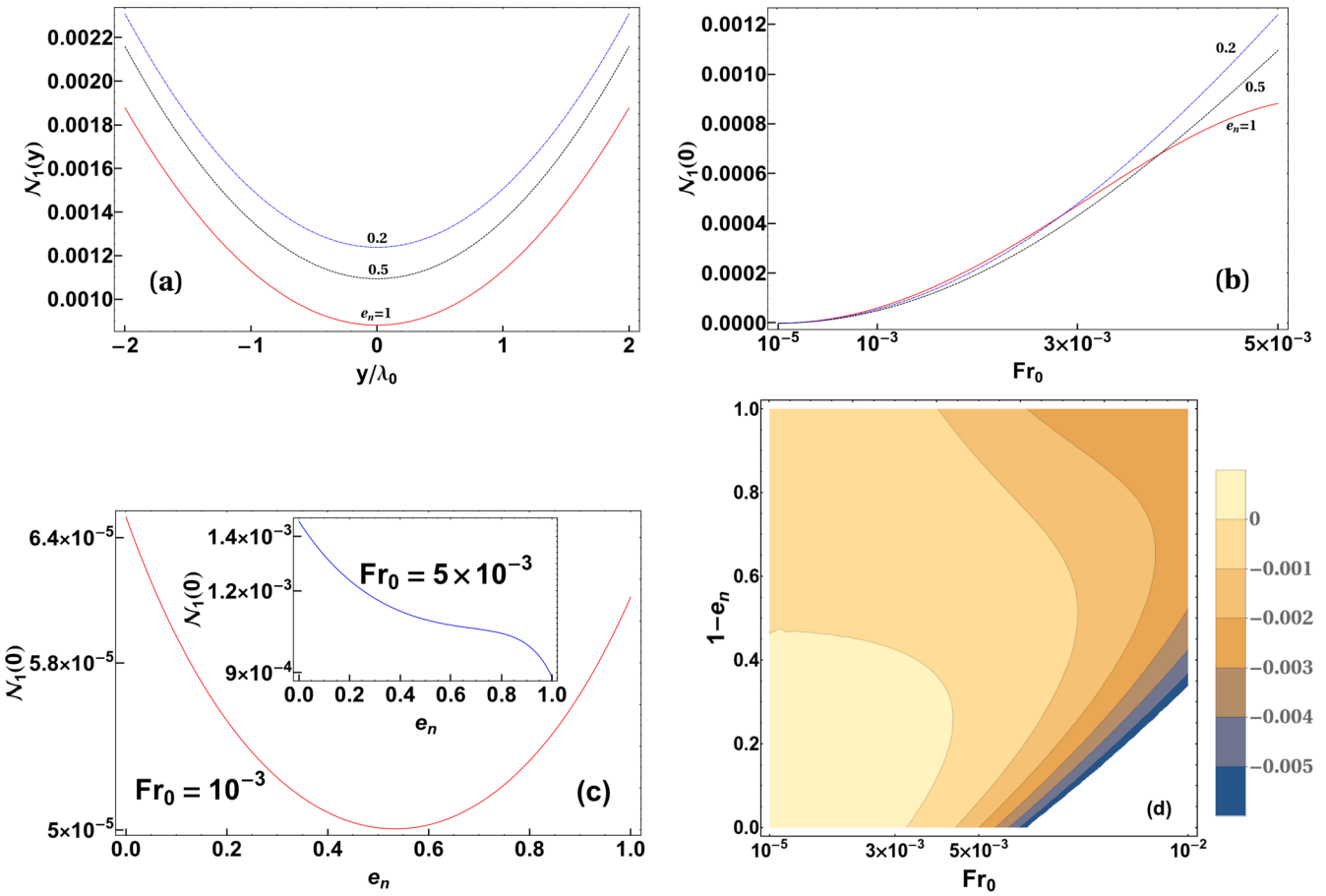

FIG. 6. (a) Profiles of the first normal-stress difference $\mathcal{N}_1(y)$ for $\mathrm{Fr}_0 = 5 \times 10^{-3}$ for different values of $e_n = 1$ (bottom red curve), 0.5 (middle black curve), and 0.2 (top blue curve). (b) Variations of $\mathcal{N}_1(0)$ with Fr_0 for different e_n. (c) Variations of $\mathcal{N}_1(0)$ against e_n for $\mathrm{Fr}_0 = 10^{-3}$ (main panel) and $\mathrm{Fr}_0 = 5 \times 10^{-3}$ (inset). (d) Contours of $d\mathcal{N}_1(0)/de_n$ in the $(\mathrm{Fr}_0, 1 - e_n)$ plane; note that $d\mathcal{N}_1(0)/de_n > 0$ around the left corner (lighter shaded region) of this panel, and negative elsewhere.

which is the same as Eq. (56). The expressions for the coefficients ($A^{(2\alpha)}_{P_{xx}}$ and $B^{(2\alpha)}_{P_{xx}}$), ($A^{(0)}_{P_{yy}}$ and $B^{(0)}_{P_{yy}}$), and ($A^{(2)}_{p}$ and $B^{(2\alpha)}_{p}$) are provided in Appendix B 1. The underlined terms in the above equations represent the corresponding second-order $O(g^2)$ solution. Although the normal pressure P_{yy} does not vary along the transverse direction (since $dP_{yy}/dy = 0$), the mean pressure $p(y)$ varies along the transverse direction; the latter variation is tied to the corresponding variation of streamwise (P_{xx}) and spanwise (P_{zz}) components of the pressure tensor. In fact, the mean pressure $p(y)$ has a local minima at the channel centerline, similar to that of the temperature profile as discussed in Sec. IV; the related predictions based on Navier-Stokes theory suggest a local centerline maxima of both temperature and pressure. Therefore, both the temperature dip and the pressure dip at the channel centerline are tied to the rarefaction effects [12,15] in acceleration-driven Poiseuille flow at finite Knudsen numbers.

1. Normal-stress differences: Roles of inelasticity and rarefaction

It is easy to verify from Eqs. (67)–(69) that $P_{xx} \neq P_{yy} \neq P_{zz}$, leading to "nonzero" normal-stress differences. The first and second normal-stress differences $\mathcal{N}_1$ and $\mathcal{N}_2$ are defined with respect to mean pressure:

$$\mathcal{N}_1(y) = \frac{P_{xx} - P_{yy}}{p}, \tag{71a}$$

$$\mathcal{N}_2(y) = \frac{P_{yy} - P_{zz}}{p} \equiv \frac{P_{xx} + 2P_{yy}}{p} - 3. \tag{71b}$$

Both normal-stress differences vanish at Navier-Stokes order [42,43].

The transverse profiles of the first normal-stress difference $\mathcal{N}_1(y)$ for a Froude number $\mathrm{Fr}_0 = 5 \times 10^{-3}$ with three different values of restitution coefficient $e_n = 0.2$ (top blue line), 0.5 (middle black line), and 1 (bottom red line) are displayed in Fig. 6(a). It is seen that $\mathcal{N}_1$ increases with distance from the channel centerline $y = 0$, with its minimum being located at $y = 0$; the shape of the $\mathcal{N}_1(y)$ profile remains similar in the presence of inelastic dissipation, and the effect of inelasticity is to increase the value of $\mathcal{N}_1(y)$ at this value of the Froude number. The effect of Froude number (i.e., increasing rarefaction) is illustrated in Fig. 6(b) which shows the variation of the centerline $\mathcal{N}_1(0)$ with Fr_0 for three values of restitution coefficient e_n. Overall, increasing Fr_0 increases the magnitude of $\mathcal{N}_1$, but the effect of e_n on $\mathcal{N}_1(0)$ seems to be nonmonotonic at smaller values of Fr_0. The latter effect

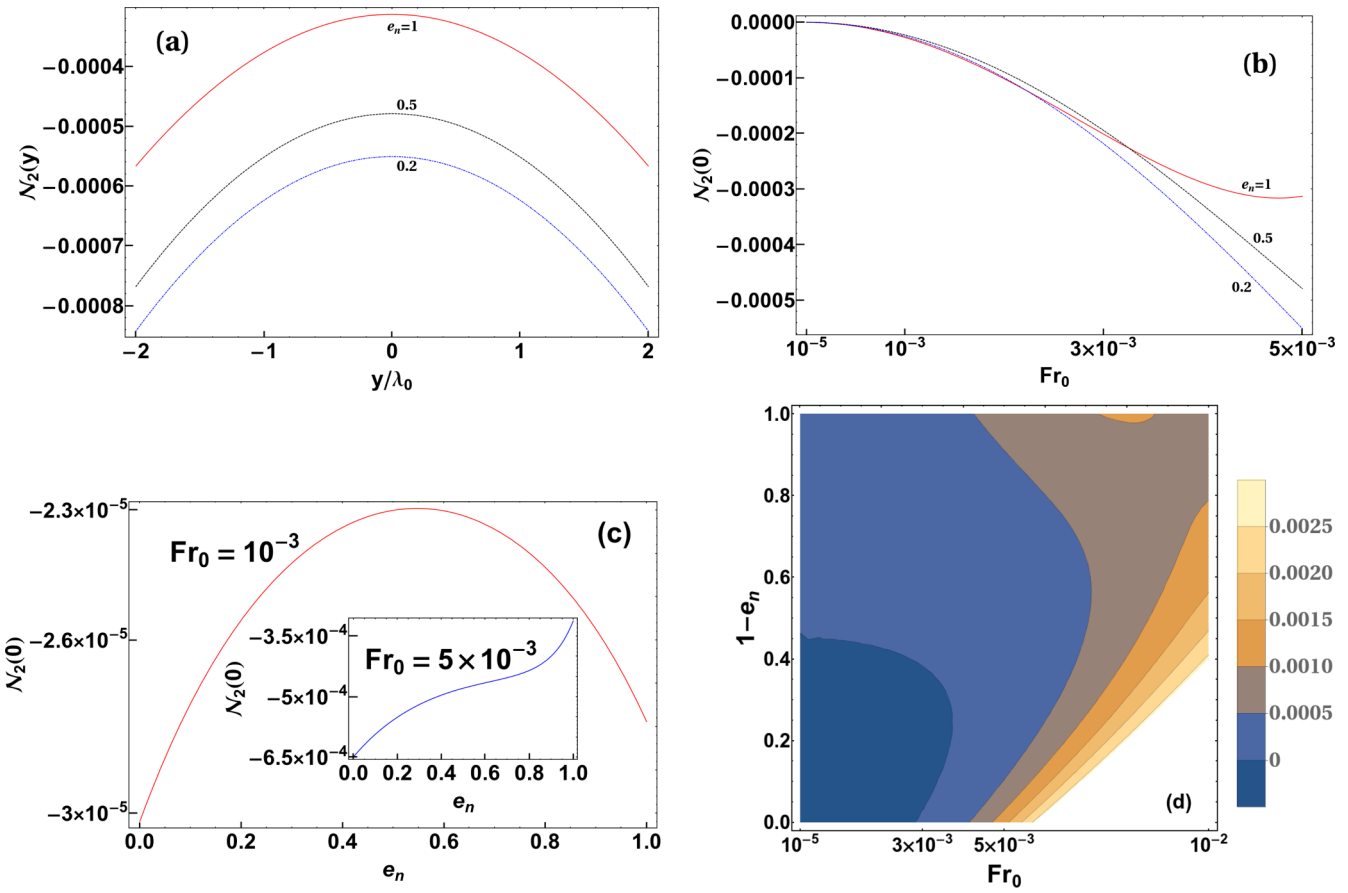

FIG. 7. Same as Fig. 6, but for the second normal-stress difference $\mathcal{N}_2$. In panels (a) and (b), different restitution coefficients refer to $e_n = 0.2$ (bottom blue line), 0.5 (middle black line), and 1 (top red line). Note that $d\mathcal{N}_2(0)/de_n < 0$ around the left corner (dark blue shaded region) of panel (d), and positive elsewhere.

is confirmed in Fig. 6(c): while the inset shows that $\mathcal{N}_1(0)$ increases monotonically with decreasing e_n at a Froude number of $\mathrm{Fr}_0 = 5 \times 10^{-3}$, the main panel ($\mathrm{Fr}_0 = 10^{-3}$) shows that $\mathcal{N}_1(0)$ decreases from the elastic limit up to a value of $e_n \sim 0.5$ and thereafter increases with further decrease of e_n. The above transition from "nonmonotonic" to "monotonic" dependence of $\mathcal{N}_1(0)$ with e_n can be understood from Fig. 6(d) which displays the contour map of the derivative of $\mathcal{N}_1(0)$ with respect to e_n [i.e., $d\mathcal{N}_1(0)/de_n$] in the $(\mathrm{Fr}_0, 1 - e_n)$ plane. In the lower left corner of Fig. 6(d) the first normal-stress difference decreases with increasing dissipation, and increases elsewhere at any Fr_0. The value of the corresponding critical Froude number is $\mathrm{Fr}_0^c(\mathcal{N}_1) \equiv \sup_{e_n} \mathrm{Fr}_0(e_n) \approx 0.0042$, with $\mathrm{Fr}_0(e_n)$ denoting the zero contour $[d\mathcal{N}_1(0)/de_n = 0]$ in Fig. 6(d).

For the second normal-stress difference, the analog of Figs. 6(a)–6(d) is shown in Figs. 7(a)–7(d). The overall features remain the same as in the case of the first normal-stress difference, except that $\mathcal{N}_2$ has the opposite sign (negative) of $\mathcal{N}_1$ and is maximum at the channel centerline $y = 0$ and decreases as one moves away from $y = 0$. The effect of increasing Fr_0 is to increase the magnitude of $\mathcal{N}_2$ at any e_n [Fig. 7(b)], but the inelastic dissipation has a "dual" effect of increasing, or, decreasing $|\mathcal{N}_2|$ at larger and smaller values of Fr_0 [Fig. 7(c)], respectively. That there is a minimum value of the Froude number, above or below which the variation of $\mathcal{N}_2(0)$ is monotonic or nonmonotonic with e_n, is quantified in Fig. 7(d) which displays the contour map of $d\mathcal{N}_2(0)/de_n$ in the $(\mathrm{Fr}_0, 1 - e_n)$ plane: $\mathrm{Fr}_0^c(\mathcal{N}_2) \approx 0.004$.

It is straightforward to verify from Eqs. (67)–(69) that the "second-order" solution for both first and second normal-stress differences

$$\frac{[\mathcal{N}_1(y)]_{\mathrm{II}}}{\mathrm{Fr}_0^2} = \left[A^{(0)}_{P_{xx}}(e_n) - A^{(0)}_{P_{yy}}(e_n)\right] + A^{(2)}_{P_{xx}}(e_n)\left(\frac{y}{\lambda_0}\right)^2 > 0, \tag{72}$$

$$\frac{[\mathcal{N}_2(y)]_{\mathrm{II}}}{\mathrm{Fr}_0^2} = \left[A^{(0)}_{P_{xx}}(e_n) + 2A^{(0)}_{P_{yy}}(e_n)\right] + A^{(2)}_{P_{xx}}(e_n)\left(\frac{y}{\lambda_0}\right)^2 < 0. \tag{73}$$

The leading coefficients in the above expressions are nonmonotonic functions of e_n: the magnitudes of both decrease with decreasing from $e_n = 1$, reach a minimum at $e_n \sim 0.5$, and increase thereafter with further decreasing e_n. Therefore, the higher-order $[B^{(0)}_{P_{xx}}(e_n)$ at $O(\mathrm{Fr}_0^4)]$ contributions are responsible for the observed "nonmonotonic to monotonic" transition of both normal-stress differences with increasing gravitational strength (Fr_0).

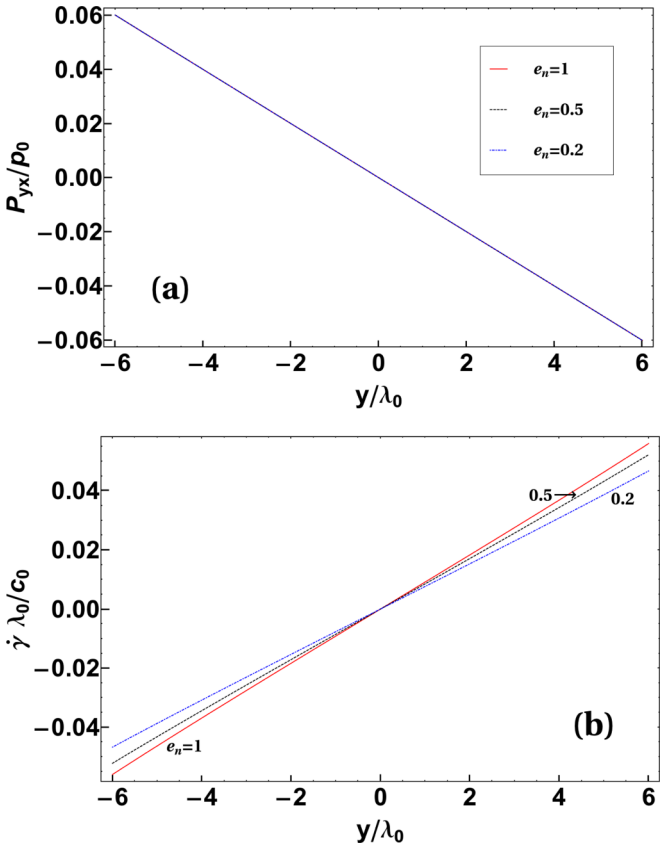

FIG. 8. Transverse profiles of (a) the shear stress (P_{yx}) and (b) the shear rate [$\dot{\gamma}(y) = du_x/dy$] for $\mathrm{Fr}_0 = 5 \times 10^{-3}$. In panel (a), different lines for $e_n = 1$, 0.5, and 0.2 overlap with each other and hence are indistinguishable.

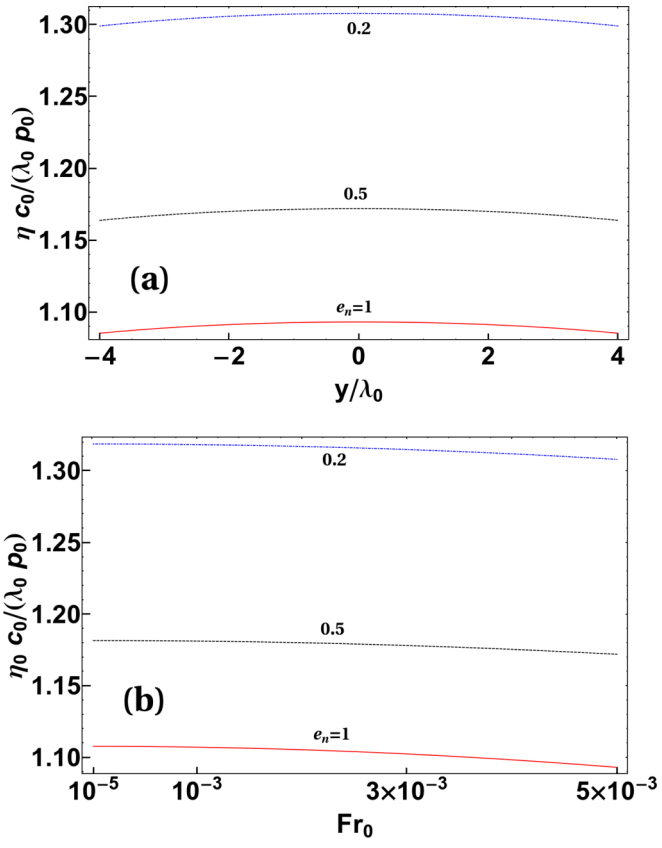

FIG. 9. (a) Transverse profiles of the shear viscosity [$\eta(y) = -P_{yx}/(du_x/dy)$] for $\mathrm{Fr}_0 = 5 \times 10^{-3}$. (b) Shear viscosity evaluated at $y = 0$ versus Froude number Fr_0. In each panel, the top, middle, and bottom curves refer to $e_n = 0.2$, 0.5, and 1, respectively.

2. Shear stress and viscosity

The expression for the shear stress P_{yx} can be written as

$$\frac{P_{yx}(y)}{p_0} = \mathrm{Fr}_0 A^{(1)}_{P_{yx}} \left(\frac{y}{\lambda_0}\right) + \mathrm{Fr}_0^3 \sum_{\alpha=1}^{2} B^{(2\alpha+1)}_{P_{yx}} \left(\frac{y}{\lambda_0}\right)^{2\alpha+1} + O\left(\mathrm{Fr}_0^5\right), \tag{74}$$

with its coefficients being given by

$$A^{(1)}_{P_{yx}} = -2, \quad B^{(3)}_{P_{yx}} = -\frac{8\left(2111 - 2329e_n + 614e_n^2\right)}{75\left(161 - 169e_n + 44e_n^2\right)}, \tag{75a}$$

$$B^{(5)}_{P_{yx}} = -\frac{16(3 - e_n)(1 + e_n)^2(23 - 11e_n)}{5625\pi}. \tag{75b}$$

Figure 8(a) shows the transverse profiles of shear stress across the channel width for different values of the restitution coefficient (e_n) at a Froude number of $\mathrm{Fr}_0 = 5 \times 10^{-3}$; each profile is nearly linear in y and the effect of e_n is not visible in this scale.

To calculate shear viscosity, we need to determine the local (dimensionless) shear rate which is given by

$$\dot{\gamma}(y) = \frac{du_x}{dy} = \frac{du_x^{(\mathrm{I})}}{dy} + \frac{du_x^{(\mathrm{III})}}{dy} + O\left(\mathrm{Fr}_0^5\right), \tag{76}$$

where

$$u_x^{(\mathrm{I})} = \mathrm{Fr}_0 A^{(2)}_{u_x} \left(\frac{y}{\lambda_0}\right)^2, \quad u_x^{(\mathrm{III})} = \mathrm{Fr}_0^3 \sum_{\alpha=1}^{3} B^{(2\alpha)}_{u_x} \left(\frac{y}{\lambda_0}\right)^{2\alpha}, \tag{77}$$

and the expressions for the coefficients [$A^{(2)}_{u_x}$, $B^{(2)}_{u_x}$, $B^{(4)}_{u_x}$, and $B^{(6)}_{u_x}$] are given in Appendix B 2. Transverse profiles of the shear rate are shown in Fig. 8(b), with parameter values as in Fig. 8(a). It is seen that increasing dissipation decreases the local shear rate away from the channel centerline, and consequently the shear viscosity [$\eta(y) = -P_{xy}/\dot{\gamma}(y)$] would increase with decreasing e_n as is evident from the viscosity profiles in Fig. 9(a). The latter effect mimics a similar behavior of shear viscosity with restitution coefficient in a heated granular gas [40]. The Navier-Stokes order viscosity can be calculated by retaining the leading-order terms in Eqs. (74) and (76):

$$\eta_{NS} = \frac{-A^{(1)}_{P_{yx}}}{2A^{(2)}_{u_x}} = \frac{5\sqrt{\pi}}{2(3 - e_n)(1 + e_n)} \overset{e_n=1}{=} \frac{5\sqrt{\pi}}{8}. \tag{78}$$

Figure 9(b) shows the variations of centerline shear viscosity,

$$\eta_0 \equiv \eta(y = 0) = \frac{1}{A^{(2)}_{u_x} + 2B^{(2)}_{u_x}\mathrm{Fr}_0^2}, \tag{79}$$

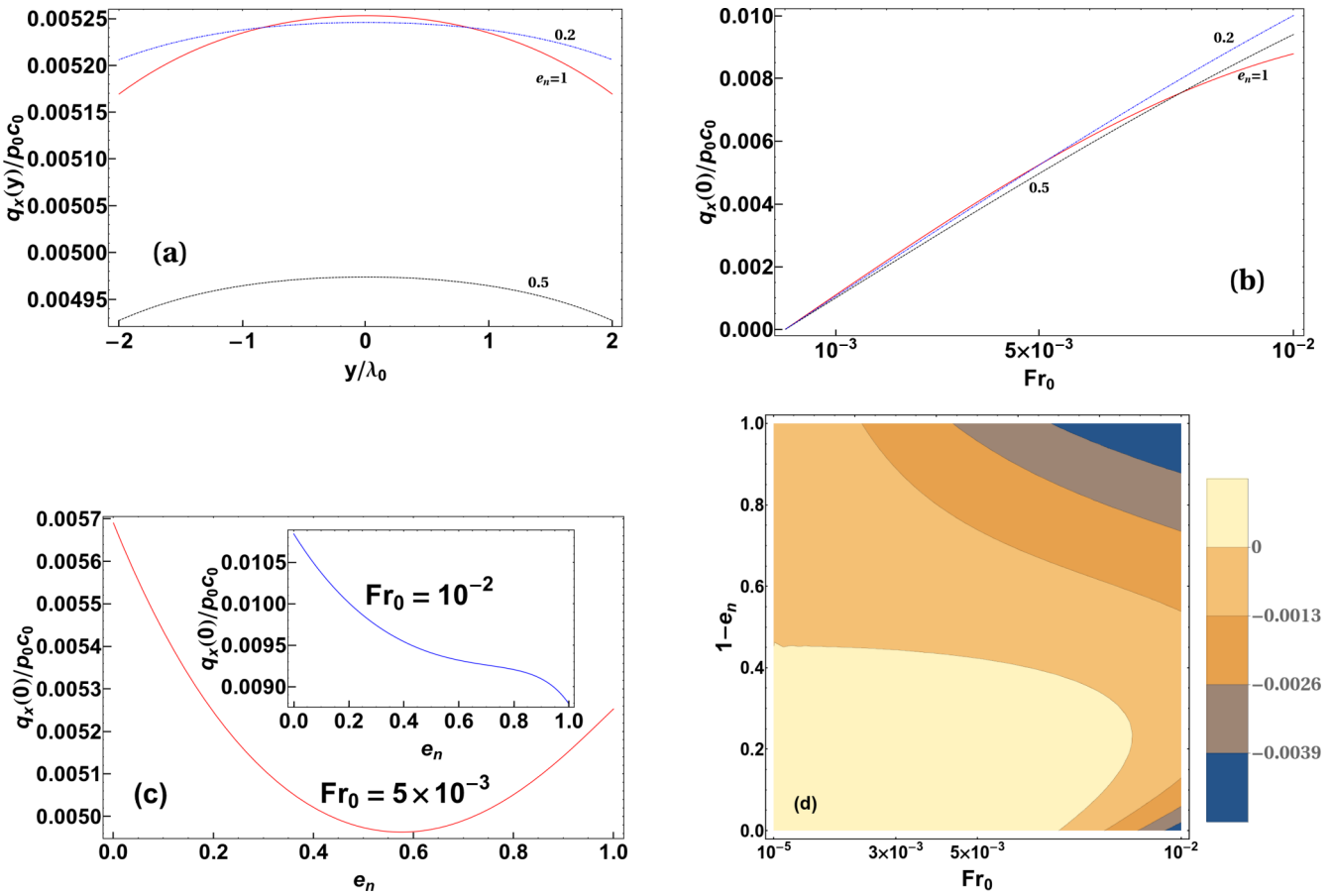

FIG. 10. (a) Profiles of dimensionless tangential heat flux ($q_x^* = q_x/p_0c_0$) at $\mathrm{Fr}_0 = 5\times10^{-3}$ for different values of e_n (as marked next to each profile). (b) Variations of $q_x(0)$ against Fr_0 for different e_n (as marked). (c) Variations of $q_x(0)$ with e_n at $\mathrm{Fr}_0 = 5\times10^{-3}$ (main panel) and $\mathrm{Fr}_0 = 10^{-2}$ (inset). (d) Contour map of $dq_x(0)/de_n$ in the $(\mathrm{Fr}_0, 1-e_n)$ plane; note that $dq_x(0)/de_n > 0$ around the left corner of this panel (lighter shaded region), and negative elsewhere.

(where $A_{u_x}^{(2)} > 0$ and $B_{u_x}^{(2)} > 0$) with Froude number Fr_0 for different e_n. The shear viscosity decreases monotonically with increasing driving strength at any e_n, confirming the shear-thinning behavior of a driven heated granular gas.

B. Tangential and normal heat fluxes: Roles of inelasticity and rarefaction

Retaining terms up to fourth order in gravitational acceleration (g), the tangential or streamwise component of heat flux (q_x) can be rewritten in terms of the centerline mean-free path (λ_0) and Froude number (Fr_0) as

$$\frac{q_x(y)}{p_0c_0} = \underline{\mathrm{Fr}_0 A_{q_x}^{(0)}} + \mathrm{Fr}_0^3 \sum_{\alpha=1}^{3} B_{q_x}^{(2\alpha-2)} \left(\frac{y}{\lambda_0}\right)^{2(\alpha-1)} + O\left(\mathrm{Fr}_0^5\right), \tag{80}$$

and the normal component of heat flux (q_y) is given by

$$\frac{q_y(y)}{p_0c_0} = \underline{\mathrm{Fr}_0^2 A_{q_y}^{(3)} \left(\frac{y}{\lambda_0}\right)^3} + \mathrm{Fr}_0^4 \sum_{\alpha=1}^{3} B_{q_y}^{(2\alpha+1)} \left(\frac{y}{\lambda_0}\right)^{2\alpha+1} + O\left(\mathrm{Fr}_0^6\right). \tag{81}$$

The expressions for the coefficients $[A_{q_x}^{(\alpha)}, B_{q_x}^{(\alpha)}]$ and $[A_{q_y}^{(\alpha)}, B_{q_y}^{(\alpha)}]$ are provided in Appendix B 3. The underlined terms in each equation above correspond to the "second-order" solution of Tij and Santos [29].

Figure 10(a) displays the profiles of dimensionless tangential heat flux $q_x(y)$ at a Froude number $\mathrm{Fr}_0 = 5\times10^{-3}$ for restitution coefficients of $e_n = 0.2$, 0.5, and 1. It is seen that $q_x(y)$ is positive and has a maximum at the channel centerline $y = 0$, and decreases away from the centerline. Figure 10(b) clarifies the dependence of $q_x(0)$ on the Froude number Fr_0; $q_x(0)$ increases significantly with increasing Froude number at any value of e_n. It is further seen that the variation of $q_x(0)$ with e_n remains monotonic [inset of Fig. 10(c)] and nonmonotonic [main panel of Fig. 10(c)] at large and small values of Fr_0, respectively; this result mimics the corresponding variations of the excess temperature ΔT [Fig. 3(a)], the first normal-stress difference $\mathcal{N}_1(0)$ [Fig. 6(c)], and the second normal-stress difference $\mathcal{N}_2(0)$ [Fig. 7(c)]. The critical Froude number for the "nonmonotonic → monotonic" transition of $q_x(0)$ as a function of e_n can be ascertained from Fig. 10(d) which shows the contour map of $dq_x(0)/de_n$ in the $(\mathrm{Fr}_0, 1-e_n)$ plane. From the phase diagrams in Figs. 5(b), 6(d), 7(d), and 10(d), we

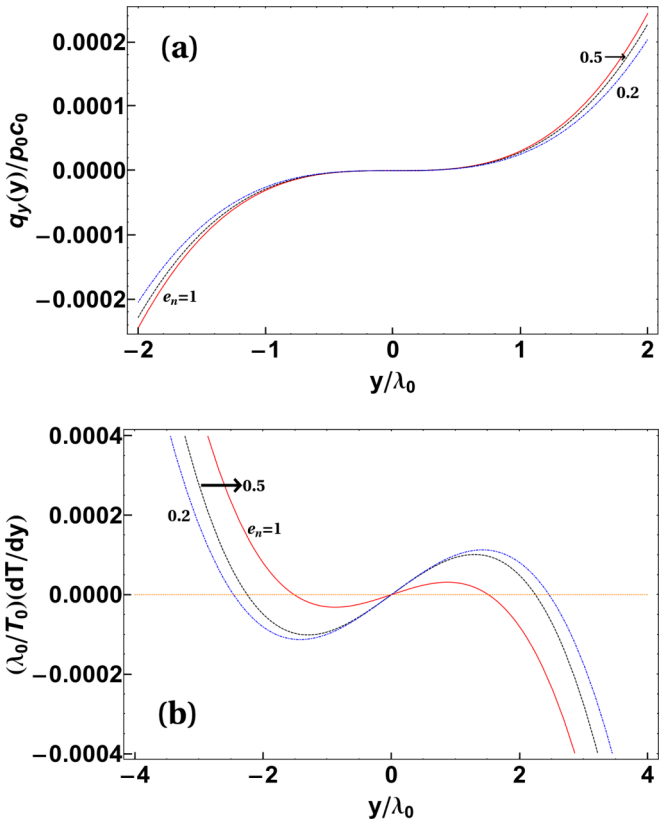

FIG. 11. Profiles of (a) the normal component of heat flux ($q_y^* = q_y/p_0c_0$) and (b) the temperature gradient (dT/dy) for $\mathrm{Fr}_0 = 5 \times 10^{-3}$. In each panel, the profiles for different restitution coefficients are marked by $e_n = 1$, 0.5, and 0.2 next to each curve.

find that

$$\mathrm{Fr}_0^c[q_x(0)] \approx 0.008 > \mathrm{Fr}_0^c[\mathcal{N}_1(0)] \approx \mathrm{Fr}_0^c[\mathcal{N}_2(0)] \approx 0.004 > \mathrm{Fr}_0^c[\Delta T] \approx 0.003; \tag{82}$$

i.e., the onset of the "nonmonotonic → monotonic" transition for $q_x(0)$ occurs at a higher value of Fr_0, compared to its value for other rarefaction metrics ($\mathcal{N}_1$, $\mathcal{N}_2$, and ΔT).

Returning to the normal component of the heat flux $q_y(y)$, Fig. 11(a) shows its transverse profiles for three restitution coefficients at $\mathrm{Fr}_0 = 5 \times 10^{-3}$. It is seen that $q_y(y)$ vanishes at the channel centerline [Eq. (81)] and is positive or negative for $y > 0$ or $y < 0$, respectively. The latter can partly be understood from the corresponding profiles of the temperature gradient dT/dy; see Fig. 11(b). According to Fourier's law, the normal heat flux obeys

$$q_y = -\kappa_{yy}\frac{dT}{dy} \Rightarrow \kappa_{yy} = -\frac{q_y}{dT/dy}, \tag{83}$$

and the positivity of thermal conductivity (κ_{yy}) dictates that q_y and dT/dy must be of opposite signs which is satisfied far away from the channel centerline at $y > y_{\max}$ [i.e., the location at which $T(y = y_{\max}) = T_{\max}$]. In fact, within the central core of the channel, spanning $-y_{\max} \leqslant y \leqslant y_{\max}$, the heat flows from the colder region [$y = 0$ at which $T(0) = T_{\min}$] to the hotter region [$|y| \leqslant y_{\max}$ at which $T(y = y_{\max}) = T_{\max}$]. This departure from Fourier's law is tied to the rarefaction or shearing effects which is also responsible for nonzero tangential heat flux.

Inserting Eqs. (81) and (59) into Eq. (83), the expression for normal thermal conductivity is found as

$$\begin{aligned}\kappa_{yy}(y) &= -\frac{q_y}{(dT/dy)} \\ &\equiv -\frac{A_{q_y}^{(3)}}{4A_T^{(4)}}\left[1 - \frac{A_T^{(2)}}{2A_T^{(4)}}\left(\frac{y}{\lambda_0}\right)^{-2} + \cdots\right] \\ &= \kappa_{NS}(e_n)\left[1 + \left(\frac{y_{\max}}{y}\right)^2 + \cdots\right],\end{aligned} \tag{84}$$

where

$$\kappa_{NS}(e_n) = -\frac{A_{q_y}^{(3)}}{4A_T^{(4)}} = \frac{75\sqrt{\pi}}{4(1+e_n)(23-11e_n)} \overset{e_n=1}{=} \frac{25\sqrt{\pi}}{32} \tag{85}$$

is the dimensionless thermal conductivity at Navier-Stokes order. Note that κ_{NS} remains constant, expectedly, across the channel width since $y_{\max} \propto A_T^{(2)} \to 0$ at this order. Moreover, $\kappa_{NS}(e_n)$ increases with decreasing restitution coefficient as expected in a heated granular gas [40].

For rarefied flows, the thermal conductivity is characterized by a rank-2 tensor via the generalized Fourier law:

$$\begin{pmatrix} q_x \\ q_y \end{pmatrix} = -\begin{bmatrix} \kappa_{xx} & \kappa_{xy} \\ \kappa_{yx} & \kappa_{yy} \end{bmatrix}\begin{pmatrix} \frac{dT}{dx} \\ \frac{dT}{dy} \end{pmatrix}, \tag{86}$$

where κ_{yy} is given by Eq. (84). For the present unidirectional flow ($dT/dy \neq 0$, but $dT/dx = 0$), an expression for the cross thermal conductivity κ_{xy} can be obtained from the first equation of Eq. (86):

$$\begin{aligned}\kappa_{xy}(y) = -\frac{q_x}{(dT/dy)} &\approx \left(\frac{-A_{q_x}^{(0)}}{4A_T^{(4)}\mathrm{Fr}_0}\right) \\ &\times\left[1 + \left(\frac{y_{\max}}{y}\right)^2 + \cdots\right]\left(\frac{\lambda_0}{y}\right)^3 > 0,\end{aligned} \tag{87}$$

which agrees with its expression for a molecular gas with $e_n = 1$ [15].

Rarefaction effect such as the anomalous normal heat flux (Fig. 11) around the core of the channel where the temperature gradient opposes the heat current may have an analog in thermal conduction on harmonic chains that show gradients of local temperature opposing the heat flow as discussed by Riedler *et al.* [44]. While the latter is known to be due to the long-range character of heat transport for harmonic chains, the induced shear gradient drives (i) the anomalous normal heat current as well as (ii) the tangential heat flux in the present flow even in the absence of a temperature gradient along the tangential direction. In any case, the simulation data on both q_x and q_y for the gravity-driven Poiseuille flow of a heated or unheated granular gas are currently lacking; the present theoretical results can be compared when such data are available. On the other hand, the DSMC results for a molecular gas ($e_n = 1$) undergoing Poiseuille flow have been carried out by Uribe and Garcia [14] along with solutions of

Burnett-order equations; their heat-flux profiles look similar to those in Fig. 10(a) and Fig. 11(a).

VI. PADÉ APPROXIMANTS AND DISCUSSION

A. Padé approximants and the range of validity of present series solutions

Following our recent work [15], the Padé approximation [45] method is employed to the present series solutions to check their region of convergence. The main idea behind this method is to replace a known "truncated" power series of a function by a sequence of rational functions [46–48]; for example,

$$\mathcal{P}[M,N]\left(f(x)=\sum_{\alpha=0}^{\infty}a_\alpha x^\alpha\right)\overset{\text{def}}{=}\frac{\mathcal{A}_M(x)}{\mathcal{B}_N(x)} \tag{88}$$

is the Padé approximant of a known power series $f(x)=\sum_{\alpha=0}^{\infty}a_\alpha x^\alpha$, which can be rewritten as

$$\sum_{\alpha=0}^{\infty}a_\alpha x^\alpha=\frac{\mathcal{A}_0+\mathcal{A}_1x+\mathcal{A}_2x^2+\cdots+\mathcal{A}_Mx^M}{1+\mathcal{B}_1x+\mathcal{B}_2x^2+\cdots+\mathcal{B}_Nx^N}+O(x^{M+N+1}), \tag{89}$$

where we have chosen $\mathcal{B}_0=1$, with a total of $(M+N+1)$ unknown coefficients. To determine $M+1$ independent numerator coefficients $(\mathcal{A}_0,\ldots,\mathcal{A}_M)$ and N independent denominator coefficients $(\mathcal{B}_1,\ldots,\mathcal{B}_N)$, the first $(M+N+1)$ terms of the power series $\sum_{\alpha=0}^{\infty}a_\alpha x^\alpha$ are compared with the respective terms in the Taylor series expansion of $\mathcal{P}[M,N](x)$. The emerging rational function $\mathcal{P}[M,N](x)$, given by Eq. (89), is called a Padé approximant of order (M,N) to the given power series; if $M=N$, then $\mathcal{P}[M,M]$ is called a "diagonal" Padé approximant.

Let us consider the present series solutions for $\mathcal{N}_1(0)$, $\mathcal{N}_2(0)$, and $q_x(0)$, with each quantity being evaluated at the channel centerline,

$$\mathcal{N}_1(0)=\mathrm{Fr}_0^2\left[A^{(0)}_{P_{xx}}(e_n)-A^{(0)}_{P_{yy}}(e_n)\right]+\mathrm{Fr}_0^4\left[B^{(0)}_{P_{xx}}(e_n)-B^{(0)}_{P_{yy}}(e_n)\right], \tag{90a}$$

$$\mathcal{N}_2(0)=\mathrm{Fr}_0^2\left[A^{(0)}_{P_{xx}}(e_n)+2A^{(0)}_{P_{yy}}(e_n)\right]+\mathrm{Fr}_0^4\left[B^{(0)}_{P_{xx}}(e_n)+2B^{(0)}_{P_{yy}}(e_n)\right], \tag{90b}$$

$$\frac{q_x(0)}{p_0c_0}=\mathrm{Fr}_0A^{(0)}_{q_x}(e_n)+\mathrm{Fr}_0^3B^{(0)}_{q_x}(e_n), \tag{90c}$$

with the first and second terms in each series representing its leading- and higher-order contributions, respectively. These solutions [Eq. (90)] are displayed in Figs. 12, 13, and 14; the leading- and higher-order solutions have opposite signs at large enough value of Fr_0 for any e_n, which indicates the asymptotic nature of the power series. This oscillatory behavior can be understood by inspecting the signs of the respective coefficients of leading- and higher-order terms:

$$A^{(0)}_{P_{xx}}(e_n)-A^{(0)}_{P_{yy}}(e_n)>0,\quad B^{(0)}_{P_{xx}}(e_n)-B^{(0)}_{P_{yy}}(e_n)<0, \tag{91a}$$

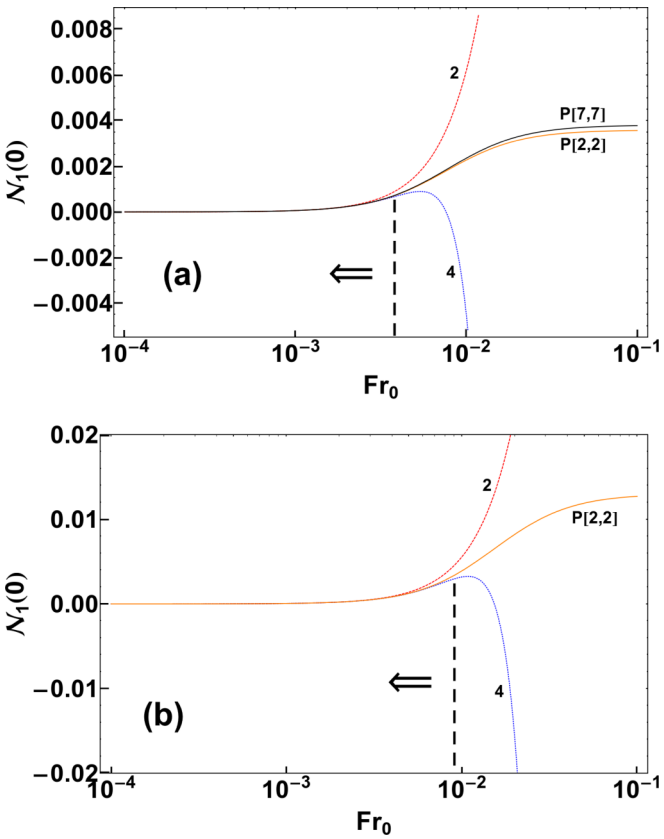

FIG. 12. Comparison of second- (top red line) and fourth-order (bottom blue line) results for the centerline first normal-stress difference $\mathcal{N}_1(0)$ with its leading-order Padé approximant (middle line) $\mathcal{P}[2,2]$ for (a) $e_n=1$ and (b) $e_n=0.2$. In panel (a), the seventh-order Padé approximant $\mathcal{P}[7,7]$ for the elastic case [15] is also superimposed.

$$A^{(0)}_{P_{xx}}(e_n)+2A^{(0)}_{P_{yy}}(e_n)<0,\quad B^{(0)}_{P_{xx}}(e_n)+2B^{(0)}_{P_{yy}}(e_n)>0, \tag{91b}$$

$$A^{(0)}_{q_x}(e_n)>0,\quad B^{(0)}_{q_x}(e_n)<0, \tag{91c}$$

which hold at any e_n as confirmed from related expressions in Appendix B.

For each power series in Eq. (90), we have calculated the leading-order Padé approximations which are messy functions of Fr_0 and e_n, see Eqs. (C1)–(C3) in Appendix C, and their expressions for a molecular gas ($e_n=1$) are given by

$$\mathcal{N}_1^{[2,2]}(0)\equiv\mathcal{P}_2^2[\mathcal{N}_1(0)](\mathrm{Fr}_0,e_n)\overset{e_n=1}{=}\frac{317\mathrm{Fr}_0^2\pi}{16\left(1+\frac{17488781\mathrm{Fr}_0^2\pi}{3170}\right)}, \tag{92}$$

$$\mathcal{N}_2^{[2,2]}(0)\equiv\mathcal{P}_2^2[\mathcal{N}_2(0)](\mathrm{Fr}_0,e_n)\overset{e_n=1}{=}-\frac{71\mathrm{Fr}_0^2\pi}{8\left(1+\frac{2492539\mathrm{Fr}_0^2\pi}{355}\right)}, \tag{93}$$

$$q_x^{[2,2]}(0)\equiv\mathcal{P}_2^2[q_x(0)](\mathrm{Fr}_0,e_n)\overset{e_n=1}{=}\frac{5\mathrm{Fr}_0\sqrt{\pi}}{8\left(1+\frac{21009\mathrm{Fr}_0^2\pi}{32}\right)}, \tag{94}$$

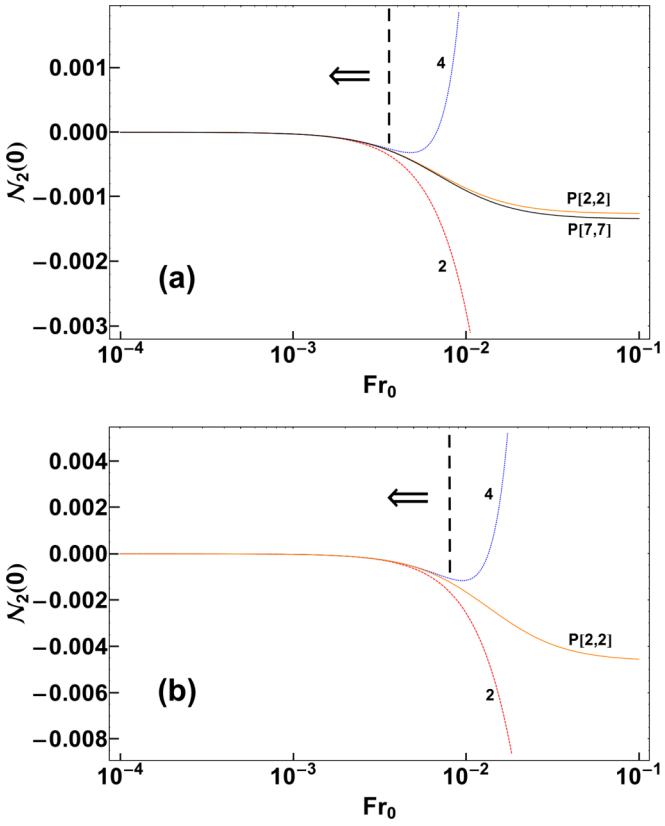

FIG. 13. Same as Fig. 12, but for the centerline second normal-stress difference $\mathcal{N}_2(0)$. In each panel, while the second-order and fourth-order solutions refer to the bottom and top lines, respectively, the middle line refers to its Padé approximant.

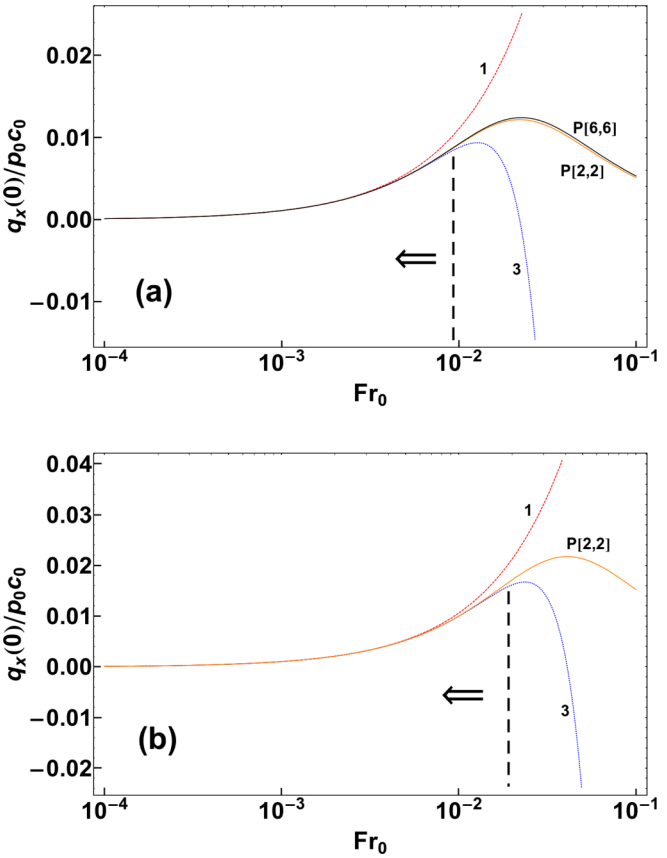

FIG. 14. Comparison of first- (top red line) and third-order (bottom blue line) results for the centerline tangential heat flux $q_x(0)$ with its Padé approximant $\mathcal{P}[2,2]$ (middle line) for (a) $e_n = 1$ and (b) $e_n = 0.2$. In panel (a), the sixth-order Padé approximant $\mathcal{P}[6,6]$ for the elastic case [15] is also superimposed.

which agrees with the second-order Padé approximants derived in our recent work [15]. Figures 12, 13, and 14 show the comparisons of Padé approximants, Eq. (C1), Eq. (C2), and Eq. (C3), respectively, with corresponding second- and fourth-order solutions. In each figure, the panel (a) represents results for a molecular gas ($e_n = 1$), while panel (b) represents a granular gas with $e_n = 0.2$. It is seen that the fourth-order solution for each rheological field closely follows its Padé approximant $\mathcal{P}[2,2]$ over a larger range of Fr_0 compared to its second-order counterpart. Comparing panels (a) and (b) of Figs. 12, 13, and 14, we find that the range of Fr_0 over which the fourth-order series solution is valid increases when inelastic dissipation is switched on; for example, the fourth-order solution for $\mathcal{N}_1(0)$ follows its Padé approximant up to $\mathrm{Fr}_0 \leqslant 5 \times 10^{-3}$ and $\mathrm{Fr}_0 \leqslant 10^{-2}$ at $e_n = 1$ and $e_n = 0.2$, respectively. Therefore, the inelasticity increases the range of validity of present higher-order series solutions in terms of Fr_0.

The influence of restitution coefficient on rarefaction effects ($\mathcal{N}_1$, $\mathcal{N}_2$, and q_x) can be understood by comparing the leading Padé approximant $\mathcal{P}[2,2]$ between panels (a) ($e_n = 1$) and (b) ($e_n = 0.2$) in Figs. 12, 13, and 14. We find that the magnitudes of $\mathcal{N}_1(0)$, $\mathcal{N}_2(0)$, and $q_x(0)$ increase significantly with increasing inelasticity at $\mathrm{Fr}_0 > 10^{-3}$.

In Figs. 12(a), 13(a), and 14(a), we have compared $\mathcal{P}[2,2]$ with respective seventh-order Padé approximant $\mathcal{P}[7,7]$ that has been recently derived by us [15] from the tenth-order perturbation solutions of a molecular gas undergoing acceleration-driven Poiseuille flow. It is seen that the leading Padé approximant $\mathcal{P}[2,2]$ closely follows its higher-order counterpart for $\mathcal{N}_1(0)$ [Fig. 12(a)], $\mathcal{N}_2(0)$ [Fig. 13(a)], and $q_x(0)$ [Fig. 14(a)]; this also provides a check on the consistency of our higher-order solutions. The agreement between $\mathcal{P}[2,2]$ and $\mathcal{P}[7,7]$ suggests that a "global" Padé approximant for each profile [$\mathcal{N}_1(y)$, $\mathcal{N}_2(y)$, $q_x(y)$, $q_y(y)$, $T(y)$, ...], based on the fourth-order solution, could be a good approximation for each field; such Padé approximated solutions are likely to be valid for larger values of Fr_0 (> 0.01) than the original fourth-order (asymptotic) series solution.

B. Qualitative comparison with simulation: Heated and unheated granular gases

In the previous section, we have established the asymptotic nature of our higher-order solutions via a comparative analysis of Padé approximants of different orders based on present series solutions. Here we discuss the similarities and differences of the present theoretical predictions of a gravity-driven heated granular gas with recent DSMC (direct simulation Monte Carlo) simulations of gravity-driven Poiseuille flow [32] of a granular gas ($e_n \leqslant 1$) without white-noise forcing. First we spell out the assumptions laid out in simulations

which have been carried out in a channel of dimensionless width $W/\sigma = 1860$, where σ is the particle diameter. The average Knudsen number, defined as

$$\mathrm{Kn} = \frac{\lambda_{av}}{W} = \frac{(\sqrt{2}\pi\rho_{av})^{-1}}{(W/\sigma)} \in (0.03, 10), \tag{95}$$

has been varied by varying the reduced density $\rho_{av} = n_{av}\sigma^3 \in (10^{-2}, 10^{-6})$; for example, the equilibrium mean-free path is $\lambda_{av} = 186\sigma$ at a reduced density of $\rho_{av} = 1.21 \times 10^{-2}$. There is another independent control parameter in simulations to characterize the body force defined via

$$\widehat{g} = \frac{gW}{\frac{2k_B T_w}{m}}, \tag{96}$$

where T_w is the wall temperature, m is the mass of a particle, and k_B is the Boltzmann constant (set to unity in simulations). All reported simulations of Gupta and Alam [32] correspond to $\widehat{g} = 0.5$ and higher, since the DSMC data were found to be noisy for $\widehat{g} < 0.5$; this is a well-known problem of the standard DSMC method [49]; see below. In contrast to simulations of "wall-bounded" planar channel flows, we have a single control parameter $\mathrm{Fr}_0 = g\lambda_0/c_0^2$ (the Froude number defined at the channel centerline $y = 0$) in the present theoretical analysis. The latter can be tied to two simulation control parameters via the following relation:

$$\widehat{g} = \frac{g\lambda_0}{c_0^2}\frac{W}{\lambda_0}\frac{T_0}{T_w} \equiv \frac{\mathrm{Fr}_0}{\mathrm{Kn}_0}\left(\frac{T_0}{T_w}\right) \Rightarrow \mathrm{Fr}_0 = \widehat{g}\mathrm{Kn}_0\left(\frac{T_w}{T_0}\right). \tag{97}$$

Assuming that $T_w \approx T_0$ and $\mathrm{Kn}_0 \approx \mathrm{Kn}$, we have $\mathrm{Fr}_0 \approx \widehat{g}\mathrm{Kn}_0 = \mathrm{Kn}_0/2$ with $\widehat{g} = 0.5$ [32]. Recalling that the present perturbation solutions hold only in the bulk region of the channel (around its centerline) and the wall effects are likely to influence the bulk at $\mathrm{Kn} \sim O(1)$, it is reasonable to assume that the present solutions are valid at $\mathrm{Kn} \sim O(0.1)$ or less which translates into an approximate upper bound of $\mathrm{Fr}_0 < 0.025$; this value falls within the range of validity of our fourth-order solutions (Figs. 12–14).

Note that the particle simulations of Refs. [31,32] correspond to $\mathrm{Fr}_0 \in (3 \times 10^{-3}, 5)$. They established that the excess temperature ΔT, the centerline values of the normal-stress differences $[\mathcal{N}_1(0), \mathcal{N}_2(0)]$, and the tangential heat flux $[q_x(0)]$ increase with (i) decreasing e_n and (ii) increasing $\widehat{g}$; these observations are similar to our predictions beyond $\mathrm{Fr}_0^c \sim 5 \times 10^{-3}$ [Eq. (82)]. On the other hand, theoretical predictions on the e_n dependence of the above quantities at $\mathrm{Fr}_0 < \mathrm{Fr}_0^c$ are qualitatively different from those found in simulations. We may conclude that the macroscopic properties of the gravity-driven Poiseuille flow of an "unheated" granular gas [31,32] are similar to those of the present theoretical predictions for a "heated" granular gas only at $\mathrm{Fr}_0 > \mathrm{Fr}_0^c$.

Another finding of simulations [32] is the competition between "dissipation-induced clustering" and "rarefaction-induced declustering" which is implicated as a nonmonotonic dependence of ΔT on Kn in the quasielastic limit (see Fig. 7(a) in Ref. [32]). Although it is not possible to isolate the effects of Kn and $\widehat{g}$ in the framework of present theory, we make use of the approximate relation (97) and substitute

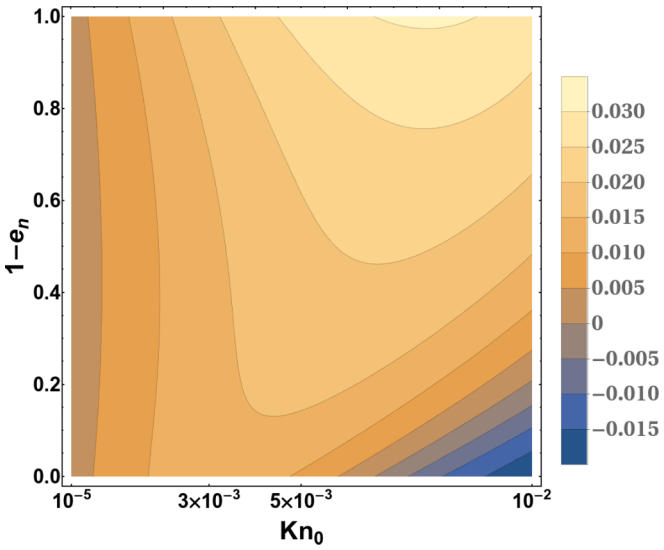

FIG. 15. Contour plot of $d\Delta T/d\mathrm{Kn}_0$ in the $(\mathrm{Kn}_0, 1 - e_n)$ plane based on the fourth-order solution for $\widehat{g} = 0.5$ and $\mathrm{Kn}_0 \approx 2\mathrm{Fr}_0$; see text in Sec. VI B for details.

it into Eq. (62) to obtain the Kn dependence of ΔT. With the above approximations, the contour plot of "$d\Delta T/d\mathrm{Kn}_0$" in the $(\mathrm{Kn}_0, 1 - e_n)$ plane is displayed in Fig. 15 based on our fourth-order solution; it is seen that the present predictions are opposite to those found in simulations [32] for an unheated granular Poiseuille flow. Clearly, certain features of the Poiseuille flow of a "heated" granular gas (especially at small Fr_0) seem to be fundamentally different from those of its unheated counterpart [31,32]. The reasons for observed differences between the present theory and previous simulation data at small values of Fr_0 or Kn could be due to the presence or absence of a bulk-heating mechanism as we discuss below.

While there is no bulk heating in the gravity-driven Poiseuille flows studied in Refs. [31,32], the stochastic white-noise term in our theoretical analysis has been added for the convenience of generating a spatially homogeneous state (in which the collisional cooling is compensated via this bulk-heating mechanism) and the gravitational acceleration is then added as a small perturbation to further analyze the dynamics of the gravity-driven Poiseuille flow of a "heated" granular gas. We speculate that for such a heated granular gas there is a threshold value for Froude number below which the "bulk heating" via white noise would dominate over gravitational acceleration, leading to different results for the variations of ΔT (and other quantities) compared to what is measured in simulations [32] for a "purely" gravity-driven granular Poiseuille flow. On the other hand, at large enough values of $\widehat{g}$, or, Fr_0, the gravitational acceleration is expected to dominate over stochastic heating and therefore the predicted results (at large $\mathrm{Fr}_0 > \mathrm{Fr}_0^c$) agree with both simulation results.

Notwithstanding the above arguments, the present theoretical predictions on the nonmonotonic variation of transport coefficients at $\mathrm{Fr}_0 < \mathrm{Fr}_0^c$ [Eq. (82)] can be checked if the simulations are carried out by incorporating the stochastic white noise in gravity-driven granular Poiseuille flow below the critical Froude number Fr_0^c. To this end, the standard DSMC simulation technique, which is not suitable at small

values of $\widehat{g}$ due to the presence of inherent noise, must be refined by employing a different or modified simulation technique (such as "variance-reduced" DSMC method [50]). This, along with an extension of the present work to dense granular gases, is left to a future work. The latter extension would provide an appropriate avenue for future verifications via experiments of gravity-driven flow of inelastic spheres, for example, down an inclined channel; the bulk heating can be imparted either via (i) small-amplitude mechanical shaking of the bottom plate on which the particles are resting, or, via (ii) electromagnetic driving [51,52], or, by employing (ii) an upward flow of a gas to energize the particles as in a fluidized bed [53]. These issues are beyond the scope of the present paper, and clearly a lot of work remains to be done from the perspectives of theory, simulation, and experiments for this simple flow configuration.

VII. IS THE PRESENT PERTURBATION EXPANSION EQUIVALENT TO CHAPMAN-ENSKOG EXPANSION?

It is interesting to find out how the series solutions based on a "nonstandard" perturbation expansion [12,29] in terms of gravitational strength (dubbed "g-based" expansion) differ from the well-known "Kn-based" Chapman-Enskog expansion [3,4,7] in terms of the gradients of hydrodynamic fields. This connection is *a priori* unclear which can be understood from the fact that (i) both the shear stress and tangential heat flux appear at first order $O(g)$ but (ii) the normal heat flux and the normal stresses are found at second order $O(g^2)$ in the present g-based expansion [see Eqs. (42) and (45)]. In contrast, the tangential heat flux as well as the normal-stress differences are known to be Burnett/second-order quantities in a gradient expansion and both vanish in the Navier-Stokes limit. It has been argued by Tij *et al.* [13] that these two expansion techniques are not equivalent; we shall show that such an equivalence can be established at the Burnett level if we consider all fourth-order terms of g-based expansion. In particular we ask, can the present series solutions for rheological fields be mapped to their Chapman-Enskog solutions? If such a mapping exists, does the second- or fourth-order solution contain all Burnett-order terms?

Recall that the closed-form analytical expressions for hydrodynamic and flux fields have been derived in terms of (i) the centerline Froude number Fr_0 and (ii) the rescaled transverse coordinate y/λ_0. Tying the Froude number with Knudsen number ($\mathrm{Fr}_0 \propto \widehat{g}\mathrm{Kn}_0$, where $\widehat{g} = mgW/2k_BT_w$ and Kn_0 is the local centerline Knudsen number [15]), one may conclude that the g-based second-order solution [$O(\mathrm{Fr}_0^2) \propto O(\mathrm{Kn}^2)$] is equivalent to the Burnett-order solution of the Chapman-Enskog method, which is incorrect as we demonstrate below; rather one needs all fourth-order $O(g^4)$ terms to establish the equivalence between the two methods. Below we analyze (i) tangential heat flux q_x and (ii) two normal-stress differences ($\mathcal{N}_1$ and $\mathcal{N}_2$) which vanish identically at the Navier-Stokes order; the goal is to express the present expressions for flux fields in terms of the gradients of hydrodynamic fields which would help to make a one-to-one comparison with related Burnett-order expressions.

Let us consider the Burnett-order expression for tangential heat flux which, for unidirectional flows [$d/dy(\cdot) \neq 0$, but $d/dx(\cdot) = 0 = d/dz(\cdot)$], is given by [3,4]

$$q_x(y) = \frac{1}{2}\frac{\theta_4\eta^2}{\rho(y)}\frac{d^2u_x}{dy^2} + \frac{3}{2}\frac{\theta_5\eta^2}{p(y)}\frac{du_x}{dy}\frac{dT}{dy} + \frac{1}{2}\frac{\theta_3\eta^2}{\rho(y)p(y)}\frac{du_x}{dy}\frac{dp}{dy}, \tag{98}$$

where the θ_i are constants. From Eq. (54), we have $u_x(y) \propto gy^2 + \cdots$, and therefore the first term of Eq. (98) yields $q_x \propto g$ at leading order which tallies with that found in Eq. (42). Now assuming that our expression for tangential heat flux q_x, Eq. (80), can be put in a form as in Eq. (98), and employing the hydrodynamic profiles in Eqs. (54)–(56) and after tedious algebra, we obtain

$$q_x(y) = \underline{\alpha_1(e_n)\lambda_0^2 p_0 \frac{d^2u_x}{dy^2}} + \Big[\alpha_2(e_n)\lambda_0^2 n_0 \frac{du_x}{dy}\frac{dT}{dy} + \alpha_3(e_n)\lambda_0^2\frac{du_x}{dy}\frac{dp}{dy} + \alpha_4(e_n)\underbrace{\lambda_0^4 p_0 \frac{d^4u_x}{dy^4}}\Big] + O\left(\mathrm{Fr}_0^5\right), \tag{99}$$

where the subscript 0 refers to quantities being evaluated at the channel centerline, with

$$\alpha_1(e_n) = \frac{75\pi}{4(1+e_n)^2(23-11e_n)(3-e_n)} \overset{e_n=1}{=} \frac{25\pi}{128}, \tag{100a}$$

$$\alpha_2(e_n) = \frac{225(111-47e_n)\pi}{8(23-11e_n)^2(3-e_n)(1+e_n)^2} \overset{e_n=1}{=} \frac{25\pi}{16}, \tag{100b}$$

$$\alpha_3(e_n) \overset{e_n=1}{=} \frac{12815\pi}{198144}, \tag{100c}$$

$$\alpha_4(e_n) \overset{e_n=1}{=} -\frac{3307625\pi^2}{2113536}, \tag{100d}$$

and the expressions for $\alpha_3(e_n)$ and $\alpha_4(e_n)$ are given in Sec. IV A of the Supplemental Material [41]. The underbraced last term in Eq. (99) is of fourth order in spatial gradients and hence represents a super-super-Burnett order term, and the remaining terms are of second order in spatial gradients and hence represent truly Burnett-order contributions. It has been verified that the underlined term in Eq. (99) has contributions from $O(\mathrm{Fr}_0)$ and $O(\mathrm{Fr}_0^3)$ [i.e., $\alpha_1 \sim O(g) + O(g^3)$], and the remaining terms have contributions only from $O(\mathrm{Fr}_0^3)$ [i.e., $(\alpha_2, \alpha_3, \alpha_4) \sim O(g^3)$] and hence are of purely third order in gravity. Therefore, the tangential heat flux q_x, Eq. (80), with all terms up to third order $O(g^3)$, can be mapped to its corresponding Burnett-order expression.

Moving onto normal-stress differences, the related Burnett-order expressions for first ($\mathcal{N}_1 = P_{xx} - P_{yy}$) and second ($\mathcal{N}_2 = P_{yy} - P_{zz}$) normal-stress differences are given by

$$\mathcal{N}_1(y) = \mathcal{A}_1 n\lambda^2\frac{d^2T}{dy^2} + \mathcal{C}_1 n\lambda^2\left(\frac{du_x}{dy}\right)^2 + \mathcal{E}_1\lambda^2\frac{d^2p}{dy^2} + \mathcal{B}_1\left(\frac{n\lambda^2}{T}\right)\left(\frac{dT}{dy}\right)^2 + \mathcal{D}_1\left(\frac{\lambda^2}{p}\right)\left(\frac{dp}{dy}\right)^2 + \mathcal{F}_1\frac{\lambda^2}{T}\frac{dp}{dy}\frac{dT}{dy}, \tag{101}$$

$$\mathcal{N}_2(y) = \mathcal{A}_2 n\lambda^2 \frac{d^2T}{dy^2} + \mathcal{C}_2 n\lambda^2 \left(\frac{du_x}{dy}\right)^2 + \mathcal{E}_2\lambda^2 \frac{d^2p}{dy^2} + \mathcal{B}_2\left(\frac{n\lambda^2}{T}\right)\left(\frac{dT}{dy}\right)^2 + \mathcal{D}_2\left(\frac{\lambda^2}{p}\right)\left(\frac{dp}{dy}\right)^2 + \mathcal{F}_2\frac{\lambda^2}{T}\frac{dp}{dy}\frac{dT}{dy}, \tag{102}$$

where the values of constants $(\mathcal{A}_i, \mathcal{B}_i, \ldots)$ can be found in Sela and Goldhirsch [23]. Following the same procedure as that of q_x, the present series solutions for normal-stress differences can be put into

$$\mathcal{N}_1(y) = \underline{\left[A_1 n_0\lambda_0^2 \frac{d^2T}{dy^2} + C_1 n_0\lambda_0^2\left(\frac{du_x}{dy}\right)^2 + E_1\lambda_0^2\frac{d^2p}{dy^2}\right]} + B_1\frac{n_0\lambda_0^2}{T_0}\left(\frac{dT}{dy}\right)^2 + D_1\frac{\lambda_0^2}{p_0}\left(\frac{dp}{dy}\right)^2 + F_1\frac{\lambda_0^2}{T_0}\frac{dp}{dy}\frac{dT}{dy} + O\left(\mathrm{Fr}_0^6\right), \tag{103}$$

$$\mathcal{N}_2(y) = \underline{\left[A_2 n_0\lambda_0^2 \frac{d^2T}{dy^2} + C_2 n_0\lambda_0^2\left(\frac{du_x}{dy}\right)^2 + E_2\lambda_0^2\frac{d^2p}{dy^2}\right]} + B_2\frac{n_0\lambda_0^2}{T_0}\left(\frac{dT}{dy}\right)^2 + D_2\frac{\lambda_0^2}{p_0}\left(\frac{dp}{dy}\right)^2 + F_2\frac{\lambda_0^2}{T_0}\frac{dp}{dy}\frac{dT}{dy} + O\left(\mathrm{Fr}_0^6\right), \tag{104}$$

where the expressions for restitution-dependent coefficients $[A_i(e_n), B_i(e_n), \ldots]$ are too cumbersome to be reproduced here, but have been written down in Sec. IV of the Supplemental Material [41]. Note that all terms in Eqs. (103) and (104) are second order in spatial gradients, representing true Burnett-order contributions as in Eqs. (101) and (102). We have verified that the underlined terms in Eqs. (103) and (104) have both second- and fourth-order $[O(g^2) + O(g^4)]$ contributions, but the remaining terms originate only from fourth-order $[O(g^4)]$ terms. Therefore, all fourth-order terms in the series solution of the pressure tensor are needed to map the corresponding expressions of two normal-stress differences to their Burnett-order counterparts.

Based on the above analysis we conclude that the present g-based expansion [12,15,29] is equivalent to the well-known Burnett-order Chapman-Enskog expansion if all terms up to the fourth-order $[O(g^4)]$ are incorporated in the former.

VIII. SUMMARY AND CONCLUSION

The effect of inelastic dissipation on the bulk hydrodynamics and rheology of the gravity-driven flow of a "heated" dilute granular gas has been studied by solving a pertinent kinetic model using the perturbation expansion technique. A BGK-like kinetic model [24,29] with white-noise forcing, which compensates for collisional cooling due to inelasticity, has been employed to approximate the Boltzmann collision operator. Neglecting wall effects and focusing only on the bulk region around the channel centerline, the effect of gravity was incorporated perturbatively around a "uniform" state of constant temperature and density. The perturbation analysis followed the previous work of Tij and Santos [29] on the same problem, but we went on to calculate fourth-order solutions in g that are found to have different dependencies on inelasticity and forcing from the second-order solution of Ref. [29], and the complexity of the problem has precluded us from calculating further higher-order terms. Apart from gaining an understanding of how the predictions based on higher-order solutions differ from their leading-order solution, two other goals of the present work were to (i) analyze the convergence properties of the underlying series solutions as done recently [15] for a molecular gas and (ii) check the equivalence of the gravity-based perturbation expansion with the Chapman-Enskog expansion.

The closed-form solutions for hydrodynamic (velocity and temperature) and rheological (pressure tensor and heat flux vector) fields have been used to analyze various rarefaction effects in detail: (i) the temperature bimodality, or, the excess temperature [$\Delta T = (T_{\max} - T_0)/T_0$, Eq. (62)], (ii) the normal-stress differences, and (iii) the tangential heat flux as functions of the restitution coefficient (e_n) and the Froude number Fr_0. It is shown that ΔT increases with increasing dissipation for $\mathrm{Fr}_0 \leqslant 5\times 10^{-3}$; for small enough values of Fr_0 ($< 5\times 10^{-3}$), however, a "nonmonotonic" behavior of ΔT with e_n [i.e., ΔT decreases with decreasing e_n for $e_n \in (1, 0.5)$, but increases for $e_n < 0.5$] is observed [Fig. 3(a)]. In contrast to these predictions based on the fourth-order solution, the leading (second-order) solution (Fig. 4) yielded a nonmonotonic variation of ΔT with e_n for all Fr_0 which is at variance with DSMC results [32].

A similar "nonmonotonic → monotonic" transition beyond a minimum value of Fr_0 has been found also for (i) two normal-stress differences (Figs. 6 and 7) and (ii) the tangential heat flux (Fig. 10). The results presented as phase diagrams in the $(\mathrm{Fr}_0, 1-e_n)$ plane in Figs. 5(b), 6(d), 7(d), and 10(d) can be summarized as follows: there is a critical Froude number $\mathrm{Fr}_0^c \equiv \mathrm{Fr}_0(e_n)$ above and below which the excess temperature ΔT, the first and second normal-stress differences $(\mathcal{N}_1, \mathcal{N}_2)$, and tangential heat flux q_x vary monotonically and nonmonotonically, respectively, with restitution coefficient. Overall, the inelastic dissipation plays a "dual" role of decreasing (at $\mathrm{Fr}_0 < \mathrm{Fr}_0^c$) and increasing (at $\mathrm{Fr}_0 > \mathrm{Fr}_0^c$) the values of ΔT, $\mathcal{N}_1$, and $\mathcal{N}_2$ with decreasing restitution coefficient e_n from the elastic limit. Therefore, we can conclude that the rarefaction effects in gravity-driven Poiseuille flow of a heated granular gas depend crucially on a competition between inelastic dissipation and external forcings: the inelastic dissipation competes with white-noise forcing if the Froude number is small enough ($\mathrm{Fr}_0 < \mathrm{Fr}_0^c$), but it competes with gravitational acceleration at $\mathrm{Fr}_0 > \mathrm{Fr}_0^c$ with the white-noise forcing playing a passive role. In contrast to our recent work [15] on the Poiseuille flow of a molecular gas for which both the leading- and higher-order solutions gave qualitatively similar results, the present case of the granular gas yielded qualitatively different results when the higher-order terms are included.

The convergence properties of the present series solutions have been analyzed following our recent work [15] that dealt with related issues for a molecular gas undergoing gravity-driven Poiseuille flow. A comparison between the leading- and higher-order solutions for the centerline values of $\mathcal{N}_1(0)$,

$\mathcal{N}_2(0)$, and $q_x(0)$ clearly indicate that the present series solutions are likely asymptotic. The leading Padé approximants for $\mathcal{N}_1(0)$, $\mathcal{N}_2(0)$, and $q_x(0)$ have been determined; a comparative study between series solutions and Padé approximants confirmed that (i) the fourth-order solution has a larger range of validity in terms of the Froude number Fr_0 than its leading-order counterpart and (ii) the role of inelasticity is to increase this range of Fr_0. It is recommended that a global Padé approximant for each series solution be determined from the present fourth-order solutions which is likely to be applicable for larger values of Fr_0. A qualitative comparison of the present theory with related simulations [31,32] indicates that the gravity-driven Poiseuille flow of a heated granular gas could be fundamentally different from its unheated counterpart. The reasons for observed differences between theory and simulation data at small values of Fr_0 may be due to the presence of bulk-heating mechanism as discussed in Sec. VI B; this needs to be verified in a future work.

We have demonstrated that the present gravity-based expansion for Poiseuille flow is equivalent to the well-known Burnett-order Chapman-Enskog expansion [i.e., a perturbation expansion in terms of the Knudsen number or the gradients of hydrodynamic fields, up to $O(\mathrm{Kn}^2)$] if all terms up to the fourth order in gravitational acceleration [$O(g^4)$] are retained in the former.

ACKNOWLEDGMENTS

We sincerely thank Professor A. Santos for useful comments on the Ph.D. thesis of the first author, a chapter of which forms the basis of the present paper. The research work of M.A. is partly funded by the Department of Science and Technology, Government of India (Ref. DST/INT/NL/P-03/2016).

APPENDIX A: SOURCE TERMS IN EQ. (34), AND THE FORM OF DISTRIBUTION FUNCTION AT DIFFERENT ORDER

The source terms in the master equation Eq. (34) at second, third, and fourth order in g, respectively, are given by

$$\phi^{(2)} = \frac{1}{1-\zeta_0}\left[\left(1+\frac{\zeta_0}{2}u^{(1)}\right)\frac{\partial}{\partial c_x} - 2c_x\left(1+c_y\frac{\partial u^{(1)}}{\partial y}\right)\right]\Phi^{(1)} - \frac{c_y}{1-\zeta_0}\left[\frac{\partial p^{(2)}}{\partial y}+\left(c^2-\frac{5}{2}\right)\frac{\partial T^{(2)}}{\partial y}\right] + \frac{2u^{(1)}}{1-\zeta_0}\left(1+c_y\frac{\partial u^{(1)}}{\partial y}\right), \tag{A1}$$

$$\begin{aligned}\phi^{(3)} = {}& \frac{1}{1-\zeta_0}\left[\left(1+\frac{\zeta_0}{2}u^{(1)}\right)\frac{\partial}{\partial c_x} - 2c_x\left(1+c_y\frac{\partial u^{(1)}}{\partial y}\right)\right]\Phi^{(2)} + \frac{1}{1-\zeta_0}\left[\left(p^{(2)}+\frac{T^{(2)}}{2}\right)\frac{\zeta_0}{4}\frac{\partial^2}{\partial c^2} - \left(p^{(2)}-\frac{T^{(2)}}{2}\right)(1-\zeta_0)\right.\\ & -\frac{1}{2}\left(p^{(2)}-\frac{T^{(2)}}{2}\right)\zeta_0\left(\boldsymbol{c}\cdot\frac{\partial}{\partial \boldsymbol{c}}\right) + 2u^{(1)}\left(1+c_y\frac{\partial u^{(1)}}{\partial y}\right) - c_y\left\{\frac{\partial p^{(2)}}{\partial y}+\left(c^2-\frac{5}{2}\right)\frac{\partial T^{(2)}}{\partial y}\right\}\Bigg]\Phi^{(1)}\\ & +\frac{2c_x}{1-\zeta_0}\left[T^{(2)}+u^{(1)}c_y\frac{\partial T^{(2)}}{\partial y}+c_y\left(T^{(2)}\frac{\partial u^{(1)}}{\partial y}-\frac{\partial u^{(3)}}{\partial y}\right)\right],\end{aligned} \tag{A2}$$

$$\begin{aligned}\phi^{(4)} = {}& \frac{1}{1-\zeta_0}\left[\left(1+\frac{\zeta_0}{2}u^{(1)}\right)\frac{\partial}{\partial c_x} - 2c_x\left(1+c_y\frac{\partial u^{(1)}}{\partial y}\right)\right]\Phi^{(3)} + \frac{1}{1-\zeta_0}\left[\left(p^{(2)}+\frac{T^{(2)}}{2}\right)\frac{\zeta_0}{4}\frac{\partial^2}{\partial c^2} - \left(p^{(2)}-\frac{T^{(2)}}{2}\right)(1-\zeta_0)\right.\\ & -\frac{1}{2}\left(p^{(2)}-\frac{T^{(2)}}{2}\right)\zeta_0\left(\boldsymbol{c}\cdot\frac{\partial}{\partial \boldsymbol{c}}\right) + 2u^{(1)}\left(1+c_y\frac{\partial u^{(1)}}{\partial y}\right) - c_y\left\{\frac{\partial p^{(2)}}{\partial y}+\left(c^2-\frac{5}{2}\right)\frac{\partial T^{(2)}}{\partial y}\right\}\Bigg]\Phi^{(2)}\\ & +\frac{1}{1-\zeta_0}\left[\left\{\left(p^{(2)}-\frac{T^{(2)}}{2}\right)u^{(1)}+u^{(3)}\right\}\frac{\zeta_0^*}{2}\frac{\partial}{\partial c_x} + 2c_x\left\{T^{(2)}+c_y\left(u^{(1)}\frac{\partial T^{(2)}}{\partial y}+\frac{\partial u^{(1)}}{\partial y}T^{(2)}-\frac{\partial u^{(3)}}{\partial y}\right)\right\}\right]\Phi^{(1)}\\ & +\frac{1}{1-\zeta_0}\left[\left(2u^{(3)}-2T^{(2)}u^{(1)}\right)\left(1+c_y\frac{\partial u^{(1)}}{\partial y}\right) + 2c_yu^{(1)}\frac{\partial u^{(3)}}{\partial y} - c_y\left\{\frac{\partial}{\partial y}\left(p^{(4)}-\frac{p^{(2)^2}}{2}\right)\right.\right.\\ & \left.\left.+\left(c^2-\frac{5}{2}\right)\frac{\partial}{\partial y}\left(T^{(4)}-\frac{T^{(2)^2}}{2}\right)+\frac{\partial T^{(2)}}{\partial y}(u^{(1)^2}-T^{(2)}c^2)\right\}\right].\end{aligned} \tag{A3}$$

The structure of $\mathscr{A}^k\phi^{(2)}$ suggests the following functional form of the second-order distribution function:

$$\begin{aligned}\Phi^{(2)}(\boldsymbol{c};y) = {}& b_0 + b_1c_y^2 + b_2c_yy + b_3y^2 + b_4c_y^4 + b_5c_y^3y + b_6c_y^2y^2 + b_7c_yy^3 + c_x^2\left(b_8 + b_9c_y^2 + b_{10}c_yy + b_{11}y^2 + b_{12}c_y^4\right.\\ & \left.+b_{13}c_y^3y + b_{14}c_y^2y^2\right) + c^2\left(b_{15} + b_{16}c_y^2 + b_{17}c_yy + b_{18}y^2 + b_{19}c_y^4 + b_{20}c_y^3y + b_{21}c_y^2y^2 + b_{22}c_yy^3\right).\end{aligned} \tag{A4}$$

The coefficients b_i can be expressed in terms of $p_2^{(2)}$, $T_2^{(2)}$, and $T_4^{(2)}$ by inserting Eqs. (43), (A1), (A4) into Eq. (36). Section I of the Supplemental Material [41] contains the expressions of the coefficients b_i as a function of ζ_0 [Eq. (30)].

The trial distribution function at fourth order $O(g^4)$ is given by

$$\begin{aligned}\Phi^{(4)}(y,\boldsymbol{c}) = {}& d_0c_y^{12} + d_1c_x^4 + d_2 + d_3c_x^2 + c_y^2\left(d_4c_x^4 + d_5 + d_6c_x^2\right) + c_y^4\left(d_7c_x^4 + d_8c_x^2 + d_9\right) + c_y^6\left(d_{15}c_x^4 + d_{16} + d_{17}c_x^2\right)\\ & + c_z^4\left(d_{10}c_y^8 + d_{11}c_y^4 + d_{12} + d_{13}c_y^2 + d_{14}c_y^6\right) + c_y^{10}\left(d_{18}c_x^2 + d_{19}\right) + c_y^8\left(d_{20}c_x^4 + d_{21}c_x^2 + d_{22}\right) + y^7\left[d_{23}c_y^3 + d_{24}c_z^2c_y\right.\end{aligned}$$

$$
\begin{aligned}
&+c_y\left(d_{25}+d_{26}c_x^2\right)\big]+c_z^2\big[d_{27}c_y^{10}+d_{28}c_x^2+d_{29}+c_y^4\left(d_{30}c_x^2+d_{31}\right)+c_y^2\left(d_{32}c_x^2+d_{33}\right)+c_y^6\left(d_{34}c_x^2+d_{35}\right)\\
&+c_y^8\left(d_{36}c_x^2+d_{37}\right)\big]+y^2\big[d_{38}c_x^4+d_{39}c_x^2+d_{40}+d_{41}c_y^{10}+c_y^2\left(d_{42}c_x^4+d_{43}+d_{44}c_x^2\right)+c_y^4\left(d_{45}c_x^2+d_{46}c_x^4+d_{47}\right)\\
&+c_z^4\left(d_{48}c_y^4+d_{49}c_y^2+d_{50}+d_{51}c_y^6\right)+c_y^8\left(d_{52}c_x^2+d_{53}\right)+c_y^6\left(d_{54}c_x^4+d_{55}c_x^2+d_{56}\right)\\
&+c_z^2\left\{d_{57}c_x^2+d_{58}+d_{59}c_y^8+c_y^4\left(d_{60}+d_{61}c_x^2\right)+c_y^2\left(d_{62}c_x^2+d_{63}\right)+c_y^6\left(d_{64}c_x^2+d_{65}\right)\right\}\big]\\
&+y^3\big[d_{66}c_y^9+c_y\left(d_{67}+d_{68}c_x^2+d_{69}c_x^4\right)+c_z^4\left(d_{70}c_y+d_{71}c_y^3+d_{72}c_y^5\right)+c_y^5\left(d_{73}c_x^4+d_{74}c_x^2+d_{75}\right)+c_y^7\left(d_{76}+d_{77}c_x^2\right)\\
&+c_y^3\left(d_{78}c_x^4+d_{79}+d_{80}c_x^2\right)+c_z^2\left\{d_{81}c_y^7+c_y\left(d_{82}+d_{83}c_x^2\right)+c_y^5\left(d_{84}c_x^2+d_{85}\right)+c_y^3\left(d_{86}c_x^2+d_{87}\right)\right\}\big]\\
&+y^5\big[d_{88}c_y^7+c_z^4\left(d_{89}c_y+d_{90}c_y^3\right)+c_y^5\left(d_{91}c_x^2+d_{92}\right)+c_y^3\left(d_{93}c_x^4+d_{94}c_x^2+d_{95}\right)+c_y\left(d_{96}c_x^4+d_{97}+d_{98}c_x^2\right)\\
&+c_z^2\left\{d_{99}c_y^5+c_y^3\left(d_{100}c_x^2+d_{101}\right)+c_y\left(d_{102}c_x^2+d_{103}\right)\right\}\big]+y\big[d_{104}c_y^{11}+c_y\left(d_{105}c_x^4+d_{106}+d_{107}c_x^2\right)\\
&+c_z^4\left(d_{108}c_y^7+d_{109}c_y+d_{110}c_y^3+d_{111}c_y^5\right)+c_y^5\left(d_{112}c_x^4+d_{113}c_x^2+d_{114}\right)+c_y^7\left(d_{115}c_x^4+d_{116}+d_{117}c_x^2\right)\\
&+c_y^3\left(d_{118}c_x^4+d_{119}c_x^2+d_{120}\right)+c_y^9\left(d_{121}c_x^2+d_{122}\right)+c_z^2\left\{d_{123}c_y^9+c_y\left(d_{124}c_x^2+d_{125}\right)+c_y^5\left(d_{126}c_x^2+d_{127}\right)\right.\\
&\left.+c_y^3\left(d_{128}c_x^2+d_{129}\right)+c_y^7\left(d_{130}c_x^2+d_{131}\right)\right\}\big]+y^6\big[d_{132}c_x^2+d_{133}c_x^4+d_{134}+d_{135}c_y^6+c_z^4\left(d_{136}c_y^2+d_{137}\right)\\
&+c_y^4\left(d_{138}c_x^2+d_{139}\right)+c_y^2\left(d_{140}c_x^4+d_{141}c_x^2+d_{142}\right)+c_z^2\left\{d_{143}c_y^4+d_{144}+d_{145}c_x^2+c_y^2\left(d_{146}c_x^2+d_{147}\right)\right\}\big]+y^4\big[d_{148}\\
&+d_{149}c_x^4+d_{150}c_x^2+d_{151}c_y^8+c_z^4\left(d_{152}c_y^4+d_{153}c_y^2+d_{154}\right)+c_y^6\left(d_{155}c_x^2+d_{156}\right)+c_y^4\left(d_{157}c_x^4+d_{158}+d_{159}c_x^2\right)\\
&+c_y^2\left(d_{160}c_x^4+d_{161}c_x^2+d_{162}\right)+c_z^2\left\{d_{163}c_x^2+d_{164}+d_{165}c_y^6+c_y^4\left(d_{166}c_x^2+d_{167}\right)+c_y^2\left(d_{168}c_x^2+d_{169}\right)\right\}\big], \qquad \text{(A5)}
\end{aligned}
$$

with unknown coefficients d_i. Section III of the Supplemental Material [41] contains the expressions of the coefficients d_i as a function of ζ_0.

Expressions for $\beta_i(\zeta_0)$ in Eqs. (48)–(52)

The expressions for $\beta_i(\zeta_0)$, with $i = 1, 2, \ldots, 12$ appearing in Eqs. (48)–(52), are given by

$$\beta_1(\zeta_0) = 10904 + 30784\zeta_0 + 29442\zeta_0^2 + 10706\zeta_0^3 + 799\zeta_0^4 - 165\zeta_0^5, \qquad \text{(A6)}$$

$$\beta_2(\zeta_0) = 336144 + 1690880\zeta_0 + 3427496\zeta_0^2 + 3545632\zeta_0^3 + 1930569\zeta_0^4 + 495020\zeta_0^5 + 35069\zeta_0^6 - 942\zeta_0^7 + 1152\zeta_0^8, \qquad \text{(A7)}$$

$$\begin{aligned}\beta_3(\zeta_0) = {} & 50528 + 367408\zeta_0 + 1102144\zeta_0^2 + 1768792\zeta_0^3 + 1631470\zeta_0^4 + 839947\zeta_0^5\\ & + 186671\zeta_0^6 - 22797\zeta_0^7 - 20613\zeta_0^8 - 3150\zeta_0^9, \end{aligned} \qquad \text{(A8)}$$

$$\begin{aligned}\beta_4(\zeta_0) = {} & 8412320 + 55869712\zeta_0 + 151604336\zeta_0^2 + 217466256\zeta_0^3 + 177155550\zeta_0^4 + 80683559\zeta_0^5 + 17862719\zeta_0^6\\ & + 760059\zeta_0^7 - 284625\zeta_0^8 - 22086\zeta_0^9, \end{aligned} \qquad \text{(A9)}$$

$$\begin{aligned}\beta_5(\zeta_0) = {} & 1599319168 + 16962443840\zeta_0 + 80336432416\zeta_0^2 + 224669350416\zeta_0^3 + 412962839352\zeta_0^4 + 524178620364\zeta_0^5\\ & + 467685587414\zeta_0^6 + 290769190027\zeta_0^7 + 120744935798\zeta_0^8 + 29912882466\zeta_0^9 + 2824796520\zeta_0^{10}\\ & - 459960093\zeta_0^{11} - 127318068\zeta_0^{12} - 6481620\zeta_0^{13}, \end{aligned} \qquad \text{(A10)}$$

$$\begin{aligned}\beta_6(\zeta_0) = {} & 5148064 + 32818512\zeta_0 + 89374032\zeta_0^2 + 136566880\zeta_0^3 + 128589078\zeta_0^4 + 75796543\zeta_0^5 + 26372423\zeta_0^6\\ & + 4378435\zeta_0^7 + 27903\zeta_0^8 - 56070\zeta_0^9, \end{aligned} \qquad \text{(A11)}$$

$$\beta_7(\zeta_0) = \frac{\left(21144 + 70636\zeta_0 + 43978\zeta_0^2 - 2137\zeta_0^3 - 2455\zeta_0^4\right)}{(1+\zeta_0)(2+\zeta_0)^2(2+5\zeta_0)}, \qquad \text{(A12)}$$

$$\begin{aligned}\beta_8(\zeta_0) = {} & 393880320 + 5561605632\zeta_0 + 34942366336\zeta_0^2 + 129006012416\zeta_0^3 + 311212453440\zeta_0^4\\ & + 515641881312\zeta_0^5 + 599613703128\zeta_0^6 + 490133164848\zeta_0^7 + 276196369025\zeta_0^8 + 101648368600\zeta_0^9\\ & + 21034331946\zeta_0^{10} + 954252636\zeta_0^{11} - 548620335\zeta_0^{12} - 105666444\zeta_0^{13} - 4864860\zeta_0^{14}, \end{aligned} \qquad \text{(A13)}$$

$$\begin{aligned}\beta_9(\zeta_0) = {} & 1066982656 + 11957194240\zeta_0 + 58644859232\zeta_0^2 + 165729887792\zeta_0^3 + 298651532384\zeta_0^4 + 358002977288\zeta_0^5\\ & + 287936971998\zeta_0^6 + 151710315739\zeta_0^7 + 48209843396\zeta_0^8 + 6708938562\zeta_0^9 - 779555905\zeta_0^{10}\\ & - 433209456\zeta_0^{11} - 57182436\zeta_0^{12} - 2568240\zeta_0^{13}, \end{aligned} \qquad \text{(A14)}$$

$$\beta_{10}(\zeta_0) = 1562108416 + 17537832640\zeta_0 + 86542601952\zeta_0^2 + 247386118112\zeta_0^3 + 454210757024\zeta_0^4 + 560679708268\zeta_0^5 + 472406095078\zeta_0^6 + 269146497804\zeta_0^7 + 99542188931\zeta_0^8 + 21415804832\zeta_0^9 + 1710159795\zeta_0^{10} - 250281216\zeta_0^{11} - 61806996\zeta_0^{12} - 3518640\zeta_0^{13}, \tag{A15}$$

$$\beta_{11}(\zeta_0) = \frac{\left(2668 + 10388\zeta_0 + 14179\zeta_0^2 + 7782\zeta_0^3 + 1323\zeta_0^4\right)}{(1+\zeta_0)^2(2+\zeta_0)(2+3\zeta_0)},$$

$$\beta_{12}(\zeta_0) = \frac{\left(10904 + 30784\zeta_0 + 29442\zeta_0^2 + 10706\zeta_0^3 + 799\zeta_0^4 - 165\zeta_0^5\right)}{(1+\zeta_0)^2(2+\zeta_0)^3(2+3\zeta_0)}. \tag{A16}$$

APPENDIX B: COEFFICIENTS FOR COMPONENTS OF PRESSURE TENSOR AND HEAT FLUX PROFILES

1. Coefficients for the profiles of P_{xx}, P_{yy}, and p

The coefficients in Eq. (67) for the profile of the streamwise component of the pressure tensor, $P_{xx}(y)$, are given by

$$A^{(0)}_{P_{xx}} = \frac{12\left(9857 - 8848e_n + 1943e_n^2\right)\pi}{(23-11e_n)^2(3-e_n)(1+e_n)^2(7-4e_n)}, \quad A^{(2)}_{P_{xx}} = \frac{56}{5}, \tag{B1a}$$

$$\begin{aligned} B^{(0)}_{P_{xx}} &= -36\pi^2\big[5320754896044755779981 - 3587701108459700939197 6e_n + 1111159853149900421302 02e_n^2 \\ &= -2092607947555531592118 08e_n^3 + 2673081953158577061737 15e_n^4 - 2445221980355482636619 04e_n^5 \\ &\quad + 1647531897362813484885 24e_n^6 - 8276293570133883292300 8e_n^7 + 3098788890846788605142 7e_n^8 \\ &\quad - 8538024661047139191880e_n^9 + 1682007130713849816634e_n^{10} - 224255541997835773344e_n^{12} \\ &\quad + 7(2589577455921188219 - 95785574361432896e_n)e_n^{13}\big] \\ &\quad \times \big[5(43-31e_n)(23-11e_n)^5(19-13e_n)^2(11-7e_n)^3(7-4e_n)^4(3-e_n)^2(1+e_n)^4\big]^{-1}, \end{aligned} \tag{B1b}$$

$$\begin{aligned} B^{(2)}_{P_{xx}} &= -72\pi\big[297764390618121 - 1336319970806724e_n + 2645757943208795e_n^2 - 3031908723889304e_n^3 \\ &\quad + 2215160257764909e_n^4 - 1069496529175192e_n^5 + 341011922140153e_n^6 + 2\big(-34596914007360e_n^7 \\ &\quad + 4050199731259e_n^8 - 208219651654e_n^9\big)\big]\big/\big[5(23-11e_n)^4(19-13e_n)(11-7e_n)^2(7-4e_n)^3(3-e_n)(1+e_n)^2\big], \end{aligned} \tag{B1c}$$

$$B^{(4)}_{P_{xx}} = -\frac{32\left(5596639 - 6700494e_n + 2548983e_n^2 - 303352e_n^3\right)}{375(23-11e_n)^2(7-4e_n)}, \tag{B1d}$$

$$B^{(6)}_{P_{xx}} = \frac{896(3-e_n)(1+e_n)^2(23-11e_n)}{28125\pi}. \tag{B1e}$$

The coefficients in Eq. (68) for the profile of the normal component of the pressure tensor, $P_{yy}(y)$, are given by

$$A^{(0)}_{P_{yy}} = -\frac{18\left(6251 - 5689e_n + 1274e_n^2\right)\pi}{(23-11e_n)^2(3-e_n)(1+e_n)^2(7-4e_n)}, \tag{B2a}$$

$$\begin{aligned} B^{(0)}_{P_{yy}} &= 162\pi^2\big(135469168054418423868 6 - 9187336735256904042281e_n + 2863608816776633573893 7e_n^2 \\ &\quad - 5430875335102671093112 3e_n^3 + 6991121839921772519616 5e_n^4 - 6449767683647435085437 4e_n^5 \\ &\quad + 4386567530854750598759 4e_n^6 - 2226421195350799806019 8e_n^7 + 8431549531175073291912e_n^8 \\ &\quad - 2352541510274823678405e_n^9 + 4699598198949310836 29e_n^{10} - 6363552540269463563 9e_n^{11} \\ &\quad + 5233325118637887973e_n^{12} - 19735050596926473 2e_n^{13}\big) \\ &\quad \times \big[5(43-31e_n)(23-11e_n)^5(19-13e_n)^2(11-7e_n)^3(7-4e_n)^4(3-e_n)^2(1+e_n)^4\big]^{-1}. \end{aligned} \tag{B2b}$$

The coefficients in Eq. (70) for the profile of pressure $p(y)$ are given by

$$A_p^{(2)} = \frac{24}{5}, \tag{B3a}$$

$$B_p^{(2)} = 216\pi\big(-52090704728123 + 234845857387702e_n - 467424166402175e_n^2 + 538907611421082e_n^3 - 396500364588437e_n^4 + 192986974641646e_n^5 - 62112762801669e_n^6 + 12740801991190e_n^7 - 1510564387244e_n^8 + 78820425644e_n^9\big)\big[5(23-11e_n)^4(19-13e_n)(11-7e_n)^2(7-4e_n)^3(3-e_n)(1+e_n)^2\big]^{-1}, \tag{B3b}$$

$$B_p^{(4)} = -\frac{32\big(1039837 - 1282302e_n + 510189e_n^2 - 65116e_n^3\big)}{125(23-11e_n)^2(7-4e_n)}, \tag{B3c}$$

$$B_p^{(6)} = \frac{128(3-e_n)(1+e_n)^2(23-11e_n)}{9375\pi}. \tag{B3d}$$

2. Coefficients for velocity profile

The coefficients in Eq. (77) are given by

$$A_{u_x}^{(2)} = \frac{2(1+e_n)(3-e_n)\big(4347 - 4563e_n + 1188e_n^2\big)}{125(23-11e_n)(7-4e_n)\sqrt{\pi}}, \tag{B4a}$$

$$B_{u_x}^{(2)} = -\frac{12\sqrt{\pi}\big(-383782811 + 908929590e_n - 850931530e_n^2 + 393106400e_n^3 - 89456115e_n^4 + 8002882e_n^5\big)}{5(23-11e_n)^3(11-7e_n)(7-4e_n)^2(1+e_n)}, \tag{B4b}$$

$$B_{u_x}^{(4)} = \frac{2(1+e_n)(3-e_n)\big(174861 - 176679e_n + 43614e_n^2\big)}{675(23-11e_n)(7-4e_n)\sqrt{\pi}}, \tag{B4c}$$

$$B_{u_x}^{(6)} = \frac{56(23-11e_n)(1+e_n)^3(3-e_n)^2}{84375\pi^{3/2}}. \tag{B4d}$$

3. Coefficients for heat-flux (q_x and q_y) profiles

The coefficients in Eq. (80) for the profile of tangential heat flux are given by

$$A_{q_x}^{(0)} = \frac{15\sqrt{\pi}}{23 + 12e_n - 11e_n^2}, \tag{B5a}$$

$$B_{q_x}^{(0)} = -45\pi^{3/2}\big(3769555817759 - 14637241462374e_n + 24691376445453e_n^2 - 23623690330552e_n^3 + 14015159421105e_n^4 - 5277353757678e_n^5 + 1231242375563e_n^6 - 162685459956e_n^7 + 9320085144e_n^8\big) \times [2(23-11e_n)^4(19-13e_n)(11-7e_n)^2(7-4e_n)^3(3-e_n)(1+e_n)^3]^{-1}, \tag{B5b}$$

$$B_{q_x}^{(2)} = \frac{6\sqrt{\pi}\big(-176362594 + 395375060e_n - 348605095e_n^2 + 150358525e_n^3 - 31474235e_n^4 + 2522803e_n^5\big)}{5(23-11e_n)^3(11-7e_n)(7-4e_n)^2(1+e_n)}, \tag{B5c}$$

$$B_{q_x}^{(4)} = -\frac{4(3-e_n)(1+e_n)(1171-487e_n)}{75(23-11e_n)\sqrt{\pi}}. \tag{B5d}$$

The coefficients in Eq. (81) for the profile of normal heat flux are given by

$$A_{q_y}^{(3)} = \frac{8(3-e_n)(1+e_n)}{15\sqrt{\pi}}, \tag{B6a}$$

$$B_{q_y}^{(3)} = -\frac{16\sqrt{\pi}\big(-383782811 + 908929590e_n - 850931530e_n^2 + 393106400e_n^3 - 89456115e_n^4 + 8002882e_n^5\big)}{5(23-11e_n)^3(11-7e_n)(7-4e_n)^2(1+e_n)}, \tag{B6b}$$

$$B_{q_y}^{(5)} = \frac{16(3-e_n)(1+e_n)\big(33789 - 34271e_n + 8486e_n^2\big)}{625(23-11e_n)(7-4e_n)\sqrt{\pi}}, \tag{B6c}$$

$$B_{q_y}^{(7)} = \frac{32(23-11e_n)(3-e_n)^2(1+e_n)^3}{21875\pi^{3/2}}. \tag{B6d}$$

APPENDIX C: PADÉ APPROXIMANTS FOR $\mathcal{N}_1(0)$, $\mathcal{N}_2(0)$, AND $q_x(0)$

For each power series for $\mathcal{N}_1(0)$, $\mathcal{N}_2(0)$, and $q_x(0)$ in Eq. (90), we have calculated the leading-order Padé approximants which are complicated functions of the Froude number Fr_0 and the restitution coefficient e_n as given by

$$\begin{aligned}
\mathcal{N}_1^{[2,2]}(0) \equiv \mathcal{P}_2^2[\mathcal{N}_1(0)] = {} & \frac{6\left(38467-34763e_n+7708e_n^2\right)\mathrm{Fr}_0^2\pi}{(3-e_n)(23-11e_n)}\Big[1+3\mathrm{Fr}_0^2\pi\big(-228337349169871697 08136 \\
& +154440052786506155164481e_n-47995676413987710591 0837e_n^2+90730036967034671680 3723e_n^3 \\
& -11638173562246749391129 15e_n^4+10695234875993656850 13174e_n^5-72429745724949025086 5394e_n^6 \\
& +36590377898424964838779 8e_n^7-13785972359751143173 0062e_n^8+38248922914567691489 405e_n^9 \\
& -75936526404820793859 29e_n^{10}+10212308126199232674 39e_n^{11}-83354010450637626823e_n^{12} \\
& +31171525947834431 32e_n^{13})\{5(19-13e_n)^2(11-7e_n)(7-4e_n)^2 \\
& \times\left(-4962243+9715939e_n-6914577e_n^2+2125941e_n^3-238948e_n^4\right)\}^{-1}\Big]^{-1} \\
\overset{e_n=1}{=} {} & \frac{317\mathrm{Fr}_0^2\pi}{16\left(1+\frac{17488781\mathrm{Fr}_0^2\pi}{3170}\right)},
\end{aligned} \tag{C1}$$

$$\begin{aligned}
\mathcal{N}_2^{[2,2]}(0) \equiv \mathcal{P}_2^2[\mathcal{N}_2(0)] = {} & \frac{-12\left(8896-8219e_n+1879e_n^2\right)\mathrm{Fr}_0^2\pi}{(3-e_n)(23-11e_n)}\Big[1+3\mathrm{Fr}_0^2\pi\big(-687147022885290236 8193 \\
& +468090195327151269885 53e_n-14660880819490697952 0231e_n^2+27951798540368723916 8299e_n^3 \\
& -36189277027771018205 91770e_n^4+33595689349272089402 7462e_n^5-23003788804064620539 9822e_n^6 \\
& +11761497188023314961 8774e_n^7-44896056872107773575 781e_n^8+12634848931426273913 765e_n^9 \\
& -25476312483405299360 27e_n^{10}+34846418662641594740 7e_n^{11}-28972883876292674224e_n^{12} \\
& +11056555331933523 16e_n^{13})\big\{5(19-13e_n)^2(11-7e_n)(7-4e_n)^2 \\
& \times\left(-1147584+2270107e_n-1635951e_n^2+510333e_n^3-58249e_n^4\right)\big\}^{-1}\Big]^{-1} \\
\overset{e_n=1}{=} {} & -\frac{71\mathrm{Fr}_0^2\pi}{8\left(1+\frac{2492539\mathrm{Fr}_0^2\pi}{355}\right)},
\end{aligned} \tag{C2}$$

$$\begin{aligned}
q_x^{[2,2]}(0) \equiv \mathcal{P}_2^2[q_x(0)] = {} & \frac{15\mathrm{Fr}_0\sqrt{\pi}}{\left(23+12e_n-11e_n^2\right)}\Big[1+3\mathrm{Fr}_0^2\pi\left(3769555817759-14637241462374e_n+24691376445453e_n^2\right. \\
& -23623690330552e_n^3+14015159421105e_n^4-5277353757678e_n^5+1231242375563e_n^6-162685459956e_n^7 \\
& \left.+9320085144e_n^8\right)\big\{2(1+e_n)^2(11-7e_n)^2\left(57-58e_n+13e_n^2\right)\left(161-169e_n+44e_n^2\right)^3\big\}^{-1}\Big]^{-1} \\
\overset{e_n=1}{=} {} & \frac{5\mathrm{Fr}_0\sqrt{\pi}}{8\left(1+\frac{21009\mathrm{Fr}_0^2\pi}{32}\right)}.
\end{aligned} \tag{C3}$$

The corresponding expressions for a molecular gas ($e_n = 1$) are also displayed above for each Padé approximant; this agrees with the second-order Padé approximant derived in our recent work [15].

[1] J. C. Maxwell, On stresses in rarefied gases arising from inequalities of temperature, Philos. Trans. R. Soc. London **170**, 231 (1879).

[2] L. Boltzmann, *Lectures on Gas Theory* (Dover Publications, New York, 1995).

[3] S. Chapman and T. G. Cowling, *The Mathematical Theory of Non-Uniform Gases* (Cambridge University Press, Cambridge, UK, 1970).

[4] D. Burnett, The distribution velocities in a slightly non-uniform gas, Proc. Lond. Math. Soc. **39**, 385 (1935).

[5] H. Grad, On the kinetic theory of rarefied gases, Commun. Pure Appl. Math. **2**, 331 (1949).

[6] M. N. Kogan, *Rarefied Gas Dynamics* (Plenum, New York, 1969).

[7] C. Cercignani, *The Boltzmann Equation and its Applications* (Springer, New York, 1988).

[8] C. Cercignani, *Rarefied Gas Dynamics* (Cambridge University Press, Cambridge, UK, 2000).

[9] M. Knudsen, Die Gesetze der Molekularstromung und der inneren Reibungsstromung der Gase durch Rohren, Ann. Phys. **28**, 75 (1909).

[10] C. Cercignani and A. Daneri, Flow of a rarefied gas between two parallel plates, J. Appl. Phys. **34**, 3509 (1963).

[11] M. Alaoui and A. Santos, Poiseuille flow driven by an external force, Phys. Fluids. A **4**, 1273 (1992).

[12] M. Tij and A. Santos, Perturbation analysis of a stationary nonequilibrium flow generated by external force, J. Stat. Phys. **76**, 1399 (1994).

[13] M. Tij, M. Sabbane, and A. Santos, Nonlinear Poiseuille flow in a gas, Phys. Fluids **10**, 1021 (1998).

[14] F. J. Uribe and A. L. Garcia, Burnett description for plane Poiseuille flow, Phys. Rev. E **60**, 4063 (1999).

[15] R. Rongali and M. Alam, Asymptotic expansion and Padé approximants for acceleration-driven Poiseuille flow of a rarefied gas: Bulk hydrodynamics and rheology, Phys. Rev. E **98**, 012115 (2018).

[16] I. Goldhirsch, Rapid granular flows, Annu. Rev. Fluid Mech. **35**, 267 (2003).

[17] S. B. Savage and D. J. Jeffreys, The stress tensor in a granular flow at high shear rates, J. Fluid Mech. **110**, 255 (1981).

[18] P. K. Haff, Grain flow as a fluid-mechanical phenomenon, J. Fluid Mech. **134**, 401 (1983).

[19] J. T. Jenkins and M. W. Richman, Kinetic theory for plane flows of a dense gas of identical, rough, inelastic, circular disks, Phys. Fluids **28**, 3485 (1985).

[20] A. Goldsthein and M. Shapiro, Mechanics of collisional motion of granular materials. Part 1. General hydrodynamic equations, J. Fluid Mech. **282**, 75 (1995).

[21] J. J. Brey, M. J. Ruiz-Montero, and F. Moreno, Steady uniform shear flow in a low density granular gas, Phys. Rev. E **55**, 2846 (1997).

[22] T. P. C. van Noije and M. H. Ernst, Velocity distributions in homogeneous granular fluids: The free and the heated case, Granular Matter **1**, 57 (1998).

[23] N. Sela and I. Goldhirsch, Hydrodynamic equations for rapid flows of smooth inelastic spheres, to Burnett order, J. Fluid Mech. **361**, 41 (1998).

[24] J. J. Brey, J. W. Dufty, and A. Santos, Kinetic models for granular flow, J. Stat. Phys. **97**, 281 (1999).

[25] S. Saha and M. Alam, Non-Newtonian stress, collisional dissipation and heat flux in the shear flow of inelastic disks: A reduction via Grad's moment method, J. Fluid Mech. **757**, 251 (2014).

[26] S. Saha and M. Alam, Normal stress differences, their origin and constitutive relations for a sheared granular fluid, J. Fluid Mech. **795**, 549 (2016).

[27] S. Saha and M. Alam, Revisiting ignited-quenched transition and the non-Newtonian rheology of a sheared dilute gas-solid suspension, J. Fluid Mech. **833**, 206 (2017).

[28] N. V. Brilliantov and T. Pöschel, *Kinetic Theory of Granular Gases* (Oxford University Press, Oxford, 2004).

[29] M. Tij and A. Santos, Poiseuille flow in a heated granular gas, J. Stat. Phys. **117**, 901 (2004).

[30] A. Santos and M. Tij, Gravity-driven Poiseuille flow in dilute gases: Elastic and inelastic collisions, in *Modelling and Numerics of Kinetic Dissipative Systems*, edited by L. Pareschi, G. Russo, and G. Toscani (Nova Science, New York, 2006), pp. 53–67.

[31] M. Alam, A. Mahajan, and D. Sivanna, On Knudsen-minimum effect and temperature bimodality in a dilute granular Poiseuille flow, J. Fluid Mech. **782**, 99 (2015).

[32] R. Gupta and M. Alam, Hydrodynamics, wall-slip, and normal-stress differences in rarefied granular Poiseuille flow, Phys. Rev. E **95**, 022903 (2017).

[33] R. Gupta and M. Alam, Disentangling the role of athermal walls on the Knudsen paradox in molecular and granular gases, Phys. Rev. E **97**, 012912 (2018).

[34] K. C. Vijayakumar and M. Alam, Velocity distribution and the effect of wall roughness in granular Poiseuille flow, Phys. Rev. E **75**, 051306 (2007).

[35] V. K. Chikkadi and M. Alam, Slip velocity and stresses in granular Poiseuille flow via event driven simulation, Phys. Rev. E **80**, 021303 (2009).

[36] M. Alam and V. K. Chikkadi, Velocity distribution function and correlations in granular Poiseuille flow, J. Fluid Mech. **653**, 175 (2010).

[37] J. M. Montanero, V. Garzó, A. Santos, and J. J. Brey, Kinetic theory of simple granular shear flows of smooth hard spheres, J. Fluid Mech. **389**, 391 (1999).

[38] A. Santos and A. Astillero, System of elastic hard spheres which mimics the transport properties of a granular gas, Phys. Rev. E **72**, 031308 (2005).

[39] A. Santos, Transport coefficients of d-dimensional inelastic Maxwell models, Physica A **321**, 442 (2003).

[40] V. Garzo and J. M. Montanero, Transport coefficients of a heated granular gas, Physica A **313**, 336 (2002).

[41] See Supplemental Material at http://link.aps.org/supplemental/10.1103/PhysRevE.98.052144 that contains four sections where the explicit expressions for the coefficients (b_i, c_i, and d_i) of second-, third-, and fourth-order distribution functions are provided. Section IV of the Supplemental Material contains expressions for (i) $\alpha_i(e_n)$ of Eq. (100) and (ii) the coefficients (A_i, B_i, ...) in Eqs. (103) and (104).

[42] M. Alam and S. Luding, Non-Newtonian granular fluid: Simulation and theory, in *Powders and Grains*, edited by R. Garcia-Rojo, H. J. Herrmann, and S. McNamara (Balkema, Netherlands, 2005), pp. 1141–1145.

[43] M. Alam and S. Saha, Normal stress differences and beyond-Navier-Stokes hydrodynamics, EPJ Conf. Proc. **140**, 11014 (2017).

[44] Z. Rieder, J. L. Lebowitz, and E. Lieb, Properties of a harmonic crystal in a stationary nonequilibrium state, J. Math. Phys. **8**, 1073 (1967).

[45] H. Padé, Sur la representation approchee d'une fonction par des fractions rationelles, Ann. de l'Ecole Normale Superieure Suppl., pp. 1–93 (1892).

[46] C. M. Bender and S. A. Orszag, *Advanced Mathematical Methods for Scientists and Engineers: Asymptotic Methods and Perturbation Theory* (Springer, New York, 1999).

[47] G. A. Baker, Jr. and P. Graves-Morris, *Padé Approximants* (Cambridge University Press, New York, 1996).

[48] A. Pozzi, *Applications of Padé Approximation Theory in Fluid Dynamics* (World Scientific Publishing, Singapore, 1994).

[49] G. A. Bird, *Molecular Gas Dynamics and the Direct Simulation Monte Carlo of Gas Flows* (Clarendon, Oxford, 1994).

[50] L. L. Baker and N. G. Hadjiconstantinou, Variance reduction for Monte Carlo solutions of the Boltzmann equation, Phys. Fluids **17**, 051703 (2005).

[51] D. L. Blair and A. Kudrolli, Clustering transitions in vibrofluidized magnetized granular materials, Phys. Rev. E **67**, 021302 (2003).

[52] A. Snezhko, I. S. Aranson, and W. K. Kwok, Structure Formation in Electromagnetically Driven Granular Media, Phys. Rev. Lett. **94**, 108002 (2005).

[53] R. Jackson, *The Dynamics of Fluidized Particles* (Cambridge University Press, New York, 2000).